



DEGREE PROJECT IN ELECTRICAL ENGINEERING,
SECOND CYCLE, 30 CREDITS
STOCKHOLM, SWEDEN 2017

Ganymede's hydrogen corona and FUV albedo from HST/STIS images

JUAN ALDAY

KTH ROYAL INSTITUTE OF TECHNOLOGY

MASTER THESIS

**GANYMEDE'S HYDROGEN CORONA
AND FUV ALBEDO FROM HST/STIS
IMAGES**

Author:
Juan Alday

Supervisor:
Lorenz Roth

Examiner:
Tomas Karlsson

*A thesis submitted in fulfilment of the requirements
for the degree of Master of Science*

in the

Space and Plasma Physics
School of Electrical Engineering

July 2, 2017

Abstract

Ganymede, the largest moon in our Solar System, has been a target for intensive scientific research during the past decades. Since 1998, the Space Telescope Imaging Spectrograph (STIS) onboard of the Hubble Space Telescope (HST) has observed it in five different HST campaigns, operating in a wavelength range between 1150-1730 Å. The images were obtained when Ganymede was located at different orbital phase, providing information about both the trailing and leading hemispheres, and allowing for the search of potential hemispherical and time variability. Here, we analyze Ganymede's HST/STIS observations in the search for a hydrogen exosphere and the study of the far-ultraviolet (FUV) albedo at different wavelengths.

The hydrogen corona is expected to scatter sunlight at the Lyman- α wavelength (1216 Å), which is within STIS' spectral range. We analyze the observations at this particular wavelength, and derive models for the different sources of emission that are expected to contribute to the signal. We also estimate the potential extinction of Ganymede's coronal emissions in the Earth's upper atmosphere, which can be up to 85%. The comparison between the HST/STIS images and the model allows us to detect the hydrogen exosphere, which we estimate to be in a range of approximately $(2-8) \times 10^3 \text{ cm}^{-3}$. The atomic hydrogen abundance in Ganymede's atmosphere during HST campaign 13328 appears to be significantly lower, which could be related to differences in the plasma magnetospheric environment.

We study Ganymede's FUV albedo comparing the reflectance at different wavelengths, and potential difference between leading and trailing hemispheres. We find out that the trailing hemisphere is brighter than the leading side for $\lambda < 1600 \text{ Å}$. This dichotomy is opposite to the previous results reported for $\lambda > 2000 \text{ Å}$, where the leading hemisphere is actually brighter. Hence, there is a spectral inversion of Ganymede's surface reflectivity at some wavelength in the range 1600-2000 Å. We also find out that the reflectivity of the surface increases for $\lambda < 1400 \text{ Å}$, which might be related to space weathering processes on the surface.

Sammanfattning

Ganymedes är största månen i vårt Solsystem, och är ett föremål för intensiv vetenskaplig forskning under senaste decenier. Sedan 1998, STIS (Space Telescope Imaging Spectrograph) instrumentet ombord rymdteleskopet Hubble (HST) har observerat Ganymedes i UV ljus med våglängder mellan 1150 Å och 1730 Å i fem olika omgångar. Bilder av månen har tagits när Ganymedes var i olika positioner i sin bana. Detta gör det möjligt att jämföra båda hemisfärer av månen, och att undersöka eventuell tidsvariation. I denna rapport HST/STIS observationer av Ganymedes analyseras med målsättningen att undersöka månens exosfär bestående av atomär syre samt månens albedo i FUV våglängder.

Väteexosfären, också kallad korona, förväntas sprida Lyman- ljuset vid 1216 Å, som kan observeras av STIS. Observationer i denna våglängd analyseras och en modell är framtagen för olika källor som bidrar vid denna våglängd. En uppskattning görs också av en eventuell absorption av Ganymedes emissioner i Jordens övre atmosfär, som kan uppgå till 85%. Jämförelse av modellen med bilder från HST/STIS tyder på att Ganymedes har en väteexosfär med ytdensiteten av $(2-8) \times 10^3 \text{ cm}^{-3}$. Under Hubble kampanj 13328 har däremot betydligt lägre antal väteatomer detekterats, som kan bero på skillnader i magnetosfäriska omgivningen av månen jämfört med tidigare observationer.

FUV albedo av månens yta har undersökts genom jämförelser av reflektansen vid olika våglängder, inklusive eventuella skillnader mellan olika hemisfärer. Vi finner att bakre (i förhållande till rörelsen i banan, som månen är låst i) hemisfären är ljusare än främre hemisfären för $\lambda < 1600 \text{ Å}$. För längre våglängder, $\lambda > 2000 \text{ Å}$, har motsatta resultat rapporterats tidigare, där främre hemisfären var ljusare. Detta tyder på att Ganymedes ytrelektans har en spektral inversion mellan 1600-2000 Å. Vi noterar även att ytrelektansen ökar med kortare våglängd för $\lambda < 1400 \text{ Å}$, som kan bero på att ytans växelverkan med rymdpartiklar.

Acknowledgements

First of all, I would like to express my great gratitude to my supervisor, Lorenz Roth. I have learned a lot working with you, and you have helped me whenever I have needed it. I really appreciate your effort as my supervisor, and also the opportunities that you have provided me to go abroad and to attend conferences.

Also, I would like to mention all the help provided by Kurt D. Retherford and Tracy M. Becker during my stay at Southwest Research Institute. You made my stay in San Antonio really pleasant, and I really enjoyed working with you.

Of course, I need to mention my family, that has always been by my side. To my mother María Jesús, and my siblings Bego and Rafa. To my father, that taught me to be always curious and to work hard whenever I wanted to achieve something. Thanks for supporting me whenever I need it.

To all my friends, the ones back in Spain and the ones who have been with me in this Swedish adventure. Sergiete, we should have been friends since high school, but I am really glad Stockholm has put our paths together. Thank you for the great moments we have spent. Alex Marcos, we have been together two years and I have learned a lot from you, especially to do bad jokes.

For those of you that helped me directly or indirectly, many thanks.

Contents

Abstract	I
Sammanfattning	III
Acknowledgements	V
List of Figures	XI
List of Tables	XII
1 Introduction	1
2 Ganymede	3
2.1 Ganymede's orbit around Jupiter	3
2.2 Ganymede's interior	4
2.3 Ganymede's surface	5
2.4 Ganymede's atmosphere and aurora	6
3 Ganymede's HST/STIS observations	9
4 Image processing	13
4.1 Unit conversion	14
4.2 Image orientation	15
4.3 Location of the disk	17
5 Image modeling	19
5.1 Model for the reflected sunlight	20
5.1.1 Surface reflectivity at Lyman- α	21
5.1.2 Illumination phase functions	24
5.1.3 Spatial-spectral setup of STIS images	25
5.2 Model for the scattered light at Ganymede's H corona	28
5.3 Model for the foreground and background emissions	31
6 Results	33
7 Discussion	38
8 Summary	40
Appendices	42
A Radiative transfer model	44
A.1 Extinction of solar and IPM fluxes in Ganymede's H corona	44
A.2 Extinction of Ganymede's coronal emissions in the Earth's geocorona	45

B	Derivations for the radially escaping H corona	50
B.1	Density distribution function	50
B.2	Column density distribution function	51
C	Error analysis	54

List of Figures

1.1	The Galilean moons: Io, Europa, Ganymede and Callisto. The picture shows the moons to scale in order according to their distance from the planet Jupiter. Credit: NASA.	1
2.1	Sketch showing the different definitions of Ganymede’s hemispheres. A) The moon’s tidal locking makes the same region of Ganymede to coincide with the sub-Jovian hemisphere, which always faces Jupiter. B) Bombardment of Jupiter’s magnetospheric plasma will preferentially occur on Ganymede’s trailing hemisphere, which faces the upstream direction of the plasma.	4
2.2	Sketch of the Ganymede’s interior model proposed by Bland et al. (2008). The interior is differentiated into an iron core, a silicate mantle, and two ice shells surrounding a subsurface ocean.	5
2.3	Visible map of Ganymede, obtained from the USGS website (https://pubs.usgs.gov/imap/i2762/). The map is a mosaic including images from the Galileo and Voyager spacecrafts. The sub-Jovian and anti-Jovian hemispheres are centered at 0° and 180° respectively. The map shows that the leading side (0° - 180°) is brighter than the trailing (180° - 360°) at visible wavelengths. . . .	6
3.1	Sketch of the setup of the HST STIS observations from (Roth, 2012). The horizontal dispersion axis contains simultaneous spatial and spectral resolution while the cross dispersion axis contains spatial information.	10
3.2	Orbital coverage of HST campaigns used in this thesis. The different visits are color-coded as indicated in the legend shown in the lower-right part of the figure.	12
4.1	Combined HST STIS image from campaign 7939. The individual datasets with background emissions lower than 10 kR are combined. The trace of reflected sunlight (and oxygen aurora) can be observed along the x axis within the yellow lines. The geocoronal emission fills the entire slit at the hydrogen (1216 \AA) emission line.	13
4.2	Sketch showing the relevant directions and angles for the orientation of the STIS images.	15
4.3	Smoothed STIS images at 1216 and 1304 \AA for HST Campaigns 7939 and 8224. The STIS image is rotated for the direction of Jupiter north to point upwards.	16
4.4	Sketch of the method used for obtaining the exact position of Ganymede’s disk within the Lyman- α slit for HST Campaign 7939.	17

5.1	Not-to-scale sketch of the different contributions to the Lyman- α signal. The foreground emission stands for scattered light in the geocorona and in the IPM between Earth and Ganymede (brown). The solar flux is also scattered by the IPM behind Ganymede (green), which gives name to the background emission, and by Ganymede's hydrogen corona (blue). Additionally, the solar flux is reflected by the moon's icy surface (red).	19
5.2	Profile obtained by summing over 70 pixels (Ganymede diameter) along the x direction, centered at the center of the disk at Lyman- α , for the STIS campaign 7939. The dashed lines show the edges of the moon's disk. Signal decreasing towards the sides of the disk indicate the presence of atmospheric emissions. .	20
5.3	Ganymede's hemispherical albedo versus wavelength from Musacchio et al. (2017). The leading hemisphere is brighter in the MUV, but darker in the FUV.	22
5.4	Rotational phase curve of Ganymede from Hendrix et al. (2005). Longitudes from 0 to 90 represent the leading hemisphere, while from 180 to 360 they represent the trailing hemisphere.	22
5.5	Inversion of the visible images used for constructing the reflected sunlight model for the HST campaign 1979. The visible image with the STIS orientation (A) is inverted using different approaches (B-B'''). Finally, the resolution of the images is decreased (C-C''').	23
5.6	Geometric definitions for the incident and observing angles from Oren and Nayar (1994). The \hat{Z} direction is coincident with the normal direction to the surface.	25
5.7	Phase functions computed for HST Campaign 7939. A) Uniform phase function, as equation 5.1.2. B) Phase function for a Lambertian surface, described by equation 5.1.3. C) Phase function from the reflectance model of Oren and Nayar (1994), assuming a roughness parameter of 30°	26
5.8	Examples of synthetic 2D images created for HST Campaign 7939, corresponding to Approaches 5 (left) and 1 (right), with a uniform phase function. The region between the two yellow lines represents the trace of reflected sunlight along the spectrum, which is comparable to the STIS image in Figure 4.1. The red box represents a zoom of the image at Lyman- α , which is much brighter than the rest of the spectrum. At this particular wavelength the difference between the two approaches is clear.	27
5.9	Synthetic 2D images created for HST Campaign 7939, with the moon centered at Lyman- α . The letters A-C correspond to the different phase functions in Figure 5.7. The numbers 1-4 correspond to the different definitions in the inversion of the inverted visible images shown in Figure 5.5, and number 5 corresponding to the case of uniform reflectivity.	27
5.10	Radial column density as a function of subsolar latitude, from Marconi (2007). Sputtering of the surface is considered to be dominant in the polar regions (45° - 135°), whereas sublimation is more important near the subsolar point (0° - 45°)	28
5.11	A) Synthetic 2D image of the model for a radially symmetric escaping hydrogen corona for the HST campaign 7939, assuming a surface density of $n_0=4 \times 10^3 \text{ cm}^{-3}$. The coordinates are transformed such that $r=0$ coincides with the center of the moon within the Lyman- α slit. B) Profile obtained by summing over $2R_G$ pixels in the x axis with centered at $r=0$	30

5.12	Foreground estimation for the different HST Campaigns. The red line corresponds to the STIS profile obtained by summing over Ganymede's diameter in pixels along the x axis, centered at the disk at Lyman- α . The black line is the second order polynomial fitted in the regions between the dashed lines, and used for estimating the foreground emission.	31
6.1	Fits of the model including (black) and not including (dashed-black) corona and the STIS profile (red) for HST Campaign 7939. The letters A-C correspond to the different phase functions presented in section 5.1.2. The numbers 1-5 correspond to the different definitions in the inversion of the inverted visible images explained in section 5.1.1.	34
6.2	Fits of the model at Lyman- α including (blue) and not including (green) corona and the STIS profile (red) for the different HST campaigns used in this study. Error bars indicating the statistical uncertainty of the STIS profiles are included.	35
6.3	Surface density as a function of time (left) and orbital longitude (right) for the HST campaigns analyzed in this study. The black squares represent the values derived in Table 6.1. The red stars include a correction of the surface density for the extinction in the Earth's upper atmosphere.	35
6.4	Profile in the dispersion axis obtained by summing over $2R_G$ pixels in the y axis, centered at the moon's disk in the y direction. The profile obtained after the background subtraction of the STIS images (red), represents the reflected sunlight. The solar model (blue) is scaled with the albedo in the range 1410-1550 Å, which is the range between the two dashed lines.	36
6.5	Albedo at different wavelengths with respect to the sub-observer longitude. The color lines represent the best fit for equation 6.0.2 to the albedo points derived shown in Table 6.2. The right-bottom panel shows a comparison between the three fits at different wavelength ranges, which also includes the rotational curve at 260 nm from Hendrix et al. (2005).	37
A.1	Solar (top) and IPM background (bottom) line profiles expected after the extinction in Ganymede's hydrogen corona, assuming a column density of $N_H = 10^{13} \text{ cm}^{-2}$, for HST Campaign 12244 (Visit 2). The red-dashed line represents the initial line profile, while the black line represents the line profile after extinction. All Doppler shifts are accounted for.	46
A.2	Atomic hydrogen density distribution in the Earth's atmosphere for HST Campaign 7939. A) Distribution over longitude and altitude, at a constant latitude of 0 degrees. B) Distribution over longitude and latitude at a constant height of 600 km.	47
A.3	Extinction of Ganymede's Lyman- α coronal emissions as a function of time during HST campaign 12244 (V1). The three pannels show the Doppler shift between the moon and the Earth, the line-of-sight H density and the extinction during exposure time of the observations. These plots show evolution for every dataset in the visit. The datasets we consider in this thesis are shadowed in blue.	48
A.4	Extinction of Ganymede's Lyman- α coronal emissions in the Earth's upper atmosphere for HST Campaign 7939 and 13328 (V1), respectively. It can be observed that when the Doppler shift between the moon and the HST is small, Ganymede's coronal emissions will be extinct in the geocorona.	49
B.1	Geometry considered for the integration of the number density in order to obtain the line-of-sight column density.	51

List of Tables

- 3.1 Parameters of the HST/STIS observations of Ganymede analyzed in this study, using the $52'' \times 2''$ slit and the grating G140L. 11
- 5.1 Composite Lyman- α at 1 AU, corrected for the solar longitude difference between Ganymede and the Earth; photon scattering coefficient; background emission from Pryor et al. (2008); and foreground emission. 30
- 6.1 Results derived from the analysis of Ganymede’s hydrogen corona. The extinction of the coronal emissions in the Earth’s upper atmosphere is also included. 35
- 6.2 Results for the albedo at different wavelength ranges for the different HST campaigns. 37
- A.1 Results obtained from the radiative transfer model for the different HST campaigns. The presented values assume a column density in Ganymede’s hydrogen corona of $N_H = 10^{13} \text{ cm}^{-2}$, similar to the column density reported by Barth et al. (1997). 45

Chapter 1

Introduction

The Jovian System is often referred to as a miniature solar system. Jupiter, the largest planet in the Solar System, has 67 known moons. The Galilean moons - Io, Europa, Ganymede and Callisto (see Figure 1.1) -, named after the discovery of Galileo Galilei, are the four largest satellites of Jupiter, and especially interesting for scientific research.



Figure 1.1: The Galilean moons: Io, Europa, Ganymede and Callisto. The picture shows the moons to scale in order according to their distance from the planet Jupiter. Credit: NASA.

Io, the innermost of the Galilean moons, is the most volcanically active body in the solar system. The gases emanated from the volcanic eruptions are an important source for a tenuous atmosphere dominated by SO_2 , which plays an essential role in the Jovian magnetosphere. Europa, the smallest Galilean moon, appears to host fascinating phenomena such as water plumes (Roth et al., 2014), as an evidence for the presence of a subsurface ocean. Callisto is probably the most unknown of the Galilean moons. Its surface is heavily cratered, and measurements from the Galileo spacecraft show that its interior is relatively undifferentiated, as opposed to the other icy moons Ganymede and Europa. Ganymede, with a mean radius of 2634 km, is the largest moon of the Solar System. During the Galileo flybys, it was discovered to possess an internal magnetic field (Kivelson et al., 1996), being the only known moon to possess its own magnetosphere.

In this study, we analyze the Lyman- α (1215.67 Å) emission near Ganymede from observations made with the Space Telescope Imaging Spectrograph (STIS) on the Hubble Space Telescope (HST). The spectral and spatial resolution of the images allow us to study the atomic hydrogen corona around Ganymede, previously reported by Barth et al. (1997). We also analyze Ganymede's albedo at different wavelengths in the far-ultraviolet, in order to search for potential dichotomies between leading and trailing hemispheres.

In section 2 we review the main features known about Jupiter's moon Ganymede. Section 3 introduces the setup of the STIS observations, and presents all the HST campaigns used in this study. Sections 4 and 5 deal with the processing and modeling methods of the STIS images. Finally, section 6 presents the results of the study, whose implications are discussed in section 7.

Chapter 2

Ganymede

In this section, we give an overview of the current understanding we have about Jupiter's moon Ganymede. In the first part, we will introduce how Ganymede interacts with Jupiter, its surroundings, and with the other Galilean moons. Then, we will explain different characteristics of the moon, starting from the moon's interior to its atmosphere.

2.1 Ganymede's orbit around Jupiter

Jupiter, the fifth planet from the Sun, is the most massive in our Solar System, being even larger than all other planets and satellites combined. It orbits the Sun at a distance of approximately 5.2 AU, and it takes 11.86 years to complete a full orbit. Apart from its size, Jupiter is also the planet with the strongest magnetic field, being 10 times greater than the Earth's. Its magnetosphere extends 60-100 Jupiter radii ($R_J = 71492$ km) on the day side, and around 11000 Jupiter radii on the night side.

Similarly, Ganymede is the largest moon in the Solar System. It has a radius of $R_G = 2634$ km, which equals approximately 40 % of the radius of the Earth, and it is even larger than planet Mercury. Ganymede orbits Jupiter every 7.15 days, at a mean distance of $15R_J$, and in an almost circular orbit, with an eccentricity of 0.0013. The three inner Galilean moons - Io, Europa and Ganymede - orbit around Jupiter in a 1:2:4 resonance, which is known as a Laplace resonance. This means that every time Ganymede completes one full orbit, Europa completes two, and Io four.

All Galilean moons are tidally locked, meaning that the same hemisphere is always facing the planet as they rotate around it. Then, we can differentiate between two hemispheres: the sub-Jovian hemisphere, which always faces Jupiter, and the anti-Jovian, which would not be seen from a observer in the planet's surface. It is also possible to differentiate between two hemispheres in terms of the orbital trajectory: the leading hemisphere faces the upstream direction of the motion of Ganymede's orbit, while the trailing hemisphere is in the downstream direction (see Figure 2.1).

Due to Jupiter's great mass, the plasma dynamics within its magnetosphere are dominated by corotation. The magnetospheric plasma corotates Jupiter much faster than Ganymede's orbital motion. Thus, plasma bombardment will preferentially occur at Ganymede's trailing hemisphere, as it will face the upstream direction of the plasma. Jupiter's offset of $\approx 10^\circ$ between the magnetic and rotational axes makes Ganymede to be located at different magnetic latitudes at different times. In fact, Ganymede changes its position with respect to Jupiter's current sheet every 5.25 hours.

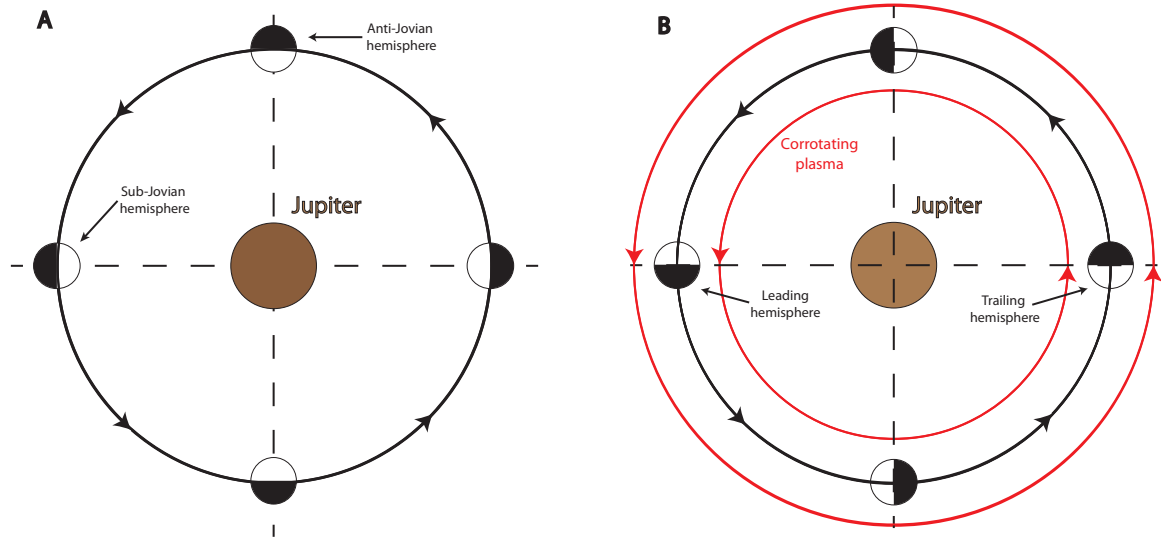


Figure 2.1: Sketch showing the different definitions of Ganymede's hemispheres. A) The moon's tidal locking makes the same region of Ganymede to coincide with the sub-Jovian hemisphere, which always faces Jupiter. B) Bombardment of Jupiter's magnetospheric plasma will preferentially occur on Ganymede's trailing hemisphere, which faces the upstream direction of the plasma.

2.2 Ganymede's interior

Gravitational data, in combination with magnetic data, allow for constraining Ganymede's interior and composition. Initial measurements made with the Pioneer and Voyager spacecrafts revealed a mean density of 1940 kg/m^3 , implying a composition of roughly 60% rock and 40% ice, that could be either uniformly mixed or differentiated. Measurements made with the Galileo spacecraft allowed for the derivation of Ganymede's moment of inertia of $C/MR^2 = 0.3105 \pm 0.0028$ (Anderson et al., 1996). The low value of the moment of inertia indicates that Ganymede is strongly differentiated, with a large concentration of mass on its center.

The detection of Ganymede's intrinsic magnetic field also implies that the moon's interior must be differentiated in a three-layer structure, with a water-ice shell, a rock mantle and a metallic core (Kivelson et al., 1996; Gurnett et al., 1996). Ganymede's magnetic field has a equatorial strength of 719 nT (Kivelson et al., 2002), which is significantly higher than the strength of Jupiter's magnetic field at Ganymede, of approximately 120 nT. Thus, Ganymede is able to produce a region where its own magnetic field dominates, being a mini-magnetosphere inside Jupiter's magnetosphere.

Kivelson et al. (2002) reported the presence of an induced magnetic field in magnetometer observations made with the Galileo spacecraft. They suggested that the source of such a field could be a subsurface ocean, although the data was also consistent with an intrinsic dipole field and additional quadrupole moments. In order to verify the existence of the subsurface ocean, Saur et al. (2015) analyzed the response of Ganymede's auroral ovals to Jupiter's time-periodic magnetic field using observations made with the Hubble Space Telescope. They showed that in the absence of a subsurface ocean, the auroral ovals should oscillate $\approx 5.8^\circ$, and $\approx 2.2^\circ$ in the presence of the ocean. The observations showed that the amplitude of the oscillation were $2.0^\circ \pm 1.3^\circ$, consistent with the presence of a subsurface ocean.

Bland et al. (2008) proposed a model for Ganymede's interior that possesses an iron core of $\approx 700 \text{ km}$, surrounded by a silicate mantle of $\approx 1000 \text{ km}$. The outer layer is formed by

a subsurface ocean, sandwiched between two ice shells (see Figure 2.2). Saur et al. (2015) suggest that the subsurface ocean is expected to lie between 150 and 250 km depth, or alternatively, in the case of a perfectly conductive ocean, at a maximum depth of 330 km.

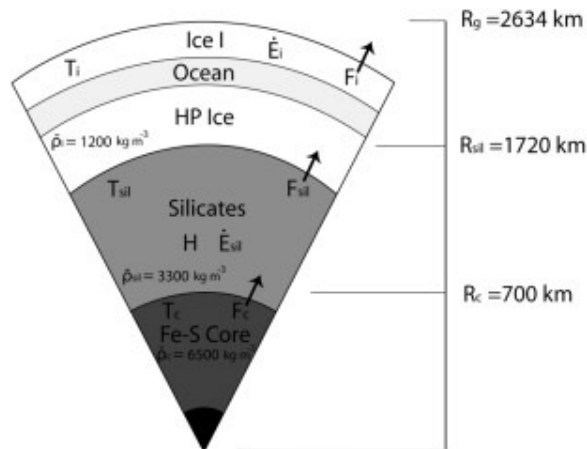


Figure 2.2: Sketch of the Ganymede's interior model proposed by Bland et al. (2008). The interior is differentiated into an iron core, a silicate mantle, and two ice shells surrounding a subsurface ocean.

2.3 Ganymede's surface

Images from the Voyager and Galileo spacecrafts show that the surface of Ganymede can be generally divided into two major types of terrain, which present differences in albedo, crater density a surface morphology (see Figure 2.3). Approximately 65% of the surface is covered by bright material, while the remaining 35% is dark. Cratering rates on both types of terrains reveals that the dark regions are older (>4 Gyr old) than the 2 to 10 times less cratered bright terrain (≈ 2 Gyr). Multispectral studies of Ganymede reveal that the bright terrains are rich in water ice, while the dark regions contain a larger fraction of rocky material (Pappalardo et al., 2004).

Prockter et al. (1998, 2000) investigated the geology of Ganymede's dark terrain using high-resolution images from the Galileo spacecraft. They suggest that the dark regions are composed of a relatively thin dark layer overlying brighter material. The albedo of dark regions is heterogeneous, what is thought to be a result of thermal segregation of ice and non-ice components (Spencer, 1987; Spencer and Robert, 1987). Geological evidence of both endogenic and exogenic processes has been observed on Ganymede's surface, like tectonism, mass wasting, sublimation and sputtering.

The bright terrains are associated with ice-rich regions, which are predominantly concentrated in the polar caps and in the visibly brighter leading hemisphere (Hansen and McCord, 2004). Galileo images also showed that Ganymede's bright terrain is heavily tectonized (Showman and Malhotra, 1999). Observations from the Galileo spacecraft show that the bright areas are generally smoother than the dark, indicating that the latter are geologically older.

Several non-ice components have also been detected on Ganymede's surface. Spectral analysis of Ganymede's surface shows that some dark regions contain hydrated minerals (Hansen and McCord, 2004; McCord et al., 2001). Other minor species have been detected on Ganymede's surface. Nelson et al. (1987) and Noll et al. (1996) reported the presence of ozone

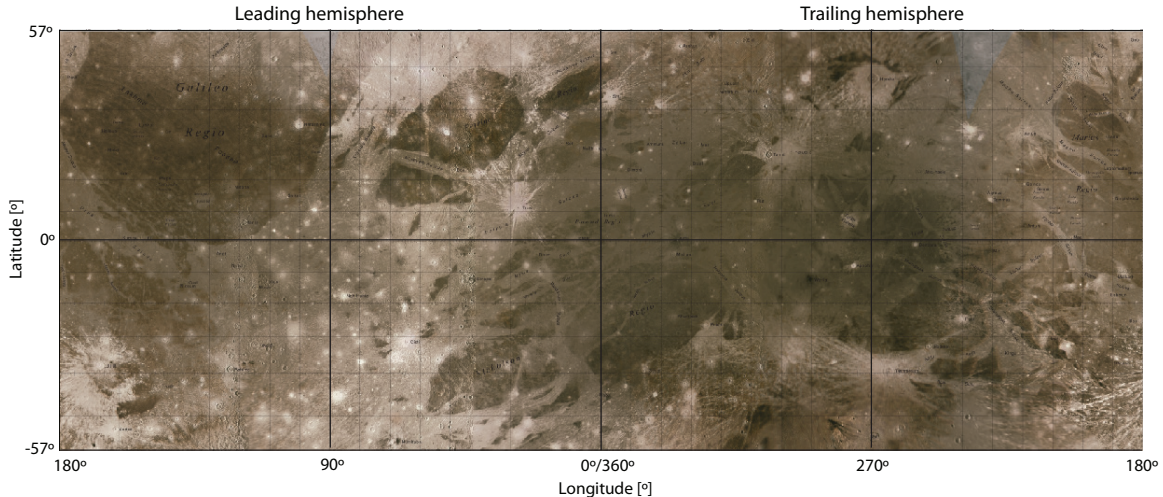


Figure 2.3: Visible map of Ganymede, obtained from the USGS website (<https://pubs.usgs.gov/imap/i2762/>). The map is a mosaic including images from the Galileo and Voyager spacecrafts. The sub-Jovian and anti-Jovian hemispheres are centered at 0° and 180° respectively. The map shows that the leading side (0° - 180°) is brighter than the trailing (180° - 360°) at visible wavelengths.

(O_3). From ground-based observations Spencer et al. (1995) detected O_2 , which appears to be predominantly concentrated on the trailing hemisphere. Carbon dioxide (CO_2) appears to be less concentrated in bright terrains, and that little or no CO_2 is detected at the poles (Hibbitts et al., 2003; McCord et al., 1997).

2.4 Ganymede's atmosphere and aurora

The first detection of Ganymede's atmosphere was made by Carlson et al. (1973) from a stellar occultation measurement. In that observation, they detected an atmosphere around Ganymede with a surface pressure of 10^{-3} mbar. The atmosphere is expected to be produced by the sublimation and sputtering of the icy surface, and thus giving rise to elements from the water species (H_2O , H_2 , O_2 , OH , O , H) (Brown et al., 1978; Lanzerotti et al., 1978; Yung and McElroy, 1977).

The first detection of auroral emissions at Ganymede was made using observations with the Goddard High Resolution Spectrograph (GHRS) on the HST (Hall et al., 1998). They reported the emission of OI 1304\AA and OI 1356\AA airglow radiation. Using the flux ratio between the two lines, they inferred an O_2 column density of $(1-10) \times 10^{14} \text{ cm}^{-2}$. Feldman et al. (2000) reported the first spatially-resolved observations of Ganymede's aurora using HST/STIS observations. They revealed that Ganymede possesses two auroral ovals similar to the ones observed on Earth, with the location of the ovals being coincident with the boundary between open and closed magnetic field lines.

Since the observation of the auroral ovals by Feldman et al. (2000), this phenomenon has been studied in different occasions. Eviatar et al. (2001) suggested that there must be a local source of acceleration for the electrons to produce the observed intensities by Feldman et al. (2000). McGrath et al. (2013) reported the hemispheric difference in latitude of the auroral ovals, which lie at higher latitudes on the orbital trailing hemisphere than on the leading. Molyneux et al. (2017), looking at the ratio between the two oxygen lines, reported that the observed ratio was consistent with an O_2 atmosphere for the leading hemisphere. Nevertheless,

the observations of the trailing hemisphere require at least 5% of atomic oxygen.

Using observations with the ultraviolet spectrometer on the Galileo spacecraft, Barth et al. (1997) reported the presence of atomic hydrogen in Ganymede's atmosphere. They analyzed the Lyman- α emission, and found that the observed signal was consistent with a hydrogen corona with a density at the surface of $1.5 \times 10^4 \text{ cm}^{-3}$. Feldman et al. (2000) analyzed the Lyman- α emission observed from HST/STIS observations made on 1998 October 30, and reported that the observed emission was in good agreement with the results proposed by Barth et al. (1997).

Using long-slit high resolution spectra, Brown (1997) analyzed the presence of sodium on Ganymede's atmosphere, which had been previously detected on Europa. However, the observations only provide an upper limit for the column density of $1 \times 10^8 \text{ cm}^{-2}$ between an altitude of 7800 and 15600 km. This value is a factor of 13 lower than for Europa's, suggesting either that Ganymede's surface is depleted in sodium compared to Europa, or that the lower sputtering rates at Ganymede (Cooper et al., 2001) impede the atmospheric sodium to be created.

Chapter 3

Ganymede's HST/STIS observations

The Space Telescope Imaging Spectrograph (STIS) is an instrument installed on board of the Hubble Space Telescope (HST), which provides spatial and spectral resolution in the ultraviolet and optical wavelength ranges. STIS counts with three different detector arrays, all providing 1024 x 1024 pixel format images:

- A CCD (charged coupled device) detector covers a field of view of $52'' \times 52''$, and a wavelength range from 2000 to 11,000 Å.
- A Cs₂ Te MAMA (multi-anode microchannel array) detector covers a field of view of $25'' \times 25''$ and operates in the near-ultraviolet (NUV), in a wavelength range from 1600 to 3100 Å.
- A CsI MAMA detector, also covering a nominal field of $25'' \times 25''$, operates in the far-ultraviolet (FUV) in a wavelength range of 1150 to 1700 Å.

In the case of this study, all the observations are made with the FUV-MAMA detector, with an aperture slit of $52'' \times 2''$ and the grating G140L (see Bostroem (2010) for further detail of the different gratings). This configuration provides images that are spatially as well as spectrally resolved, when it operates in the spectroscopic mode.

Figure 3.1 shows a sketch of the main setup of the STIS observations. The light entering the slit is dispersed in the G140L grating, separating the light in different wavelengths that will be ordered in the dispersion axis of the FUV-MAMA detector, providing spectrally resolved images. The 2'' slit width in the dispersion axis is wide enough to cover the entirety of the disk (i.e. Ganymede). In the case of the cross-dispersion axis, the 25'' aperture of the MAMA detector covers an area much larger than the size of the moon, making possible the subtraction of the background emission, as well as the study of the satellite's surroundings. This whole setup makes possible the study of the spatial information within the slit for the dominant line emissions, which are brighter than the continuum.

Hence, the spectral and spatial information are convolved in the dispersion axis. Each pixel x_d has an associated wavelength given by

$$\lambda_d = \lambda_0 + (x_d - x_0)\Delta\lambda, \quad (3.0.1)$$

where x_0 is the central pixel, λ_0 is the wavelength associated with the central pixel, and $\Delta\lambda$ is the dispersion coefficient, which are all specified in the STIS files.

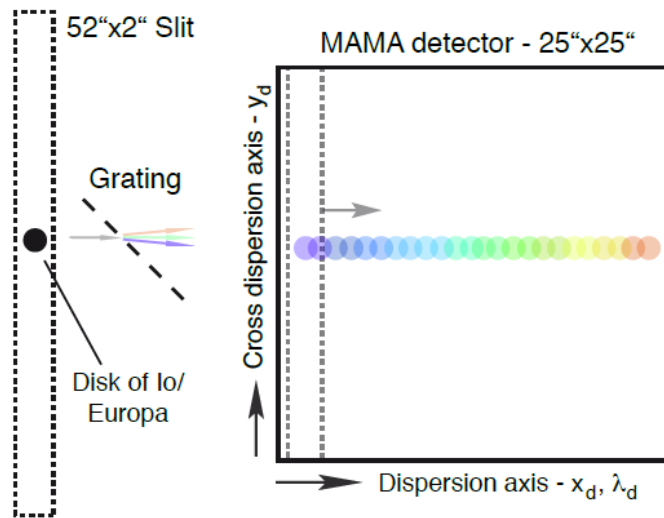


Figure 3.1: Sketch of the setup of the HST STIS observations from (Roth, 2012). The horizontal dispersion axis contains simultaneous spatial and spectral resolution while the cross dispersion axis contains spatial information.

The data files provided by the STIS have different extensions, depending on whether they are calibrated or uncalibrated. In the case of this project, the extension of the files is *flt* (flat-fielded science), which are the files corresponding to intermediate calibrated data for the MAMA detectors. The calibration procedure from the raw data to the *flt* files consists on a pixel quality check, dark current subtraction and a flat-field correction (Martin and Baltimore, 2011).

The *flt* data files consist of three different arrays and multiple headers with important information for processing the images (e.g. exposure times, telescope plate scale or dispersion coefficient). The first array contains the detector counts in each pixel $C(x_d, y_d)$, which is related to the measured flux. The second one stores the statistical errors in each pixel $\sigma_0(x_d, y_d)$. Finally, the third array has information about the functionality and quality of the pixels.

Table 3.1 shows relevant information about the HST campaigns we analyze in this study. Apart from these campaigns, Ganymede was also observed by STIS with the same experimental setup during HST Campaign 9296. However, we do not analyze that specific campaign due to the poor detected signal within the Lyman- α slit. The observations were performed away from Jupiter opposition, resulting in geocoronal emissions of approximately 22 kR [$1 \text{ R} = 10^6/4\pi \text{ photons cm}^{-2} \text{ s}^{-1} \text{ sr}^{-1}$], while in the rest of the visits presented in Table 3.1, such a contribution is between 4 and 8 kR. The strong geocoronal background makes the signal from Ganymede to be comparatively faint, and the study of a hydrogen exosphere, which is expected to emit a few hundred Rayleighs (Barth et al., 1997), is not possible.

In the observations presented on Table 3.1, Ganymede's disk extends from $1.58''$ to $1.78''$, depending on the distance between the moon and the telescope. Ganymede's position with respect to Jupiter also varies at different observations. Figure 3.2 shows a sketch indicating Ganymede's orbital longitude as seen from the HST for the different visits. The orbital coverage of the observations allows for the comparison of trailing and leading hemispheres. Besides, the observation of Ganymede at different dates, but similar orbital phases, allows for the analysis of potential time variability in the Lyman- α emission.

Table 3.1: Parameters of the HST/STIS observations of Ganymede analyzed in this study, using the $52'' \times 2''$ slit and the grating G140L.

HST Campaign ID	Dataset	Date	Start time (UTC)	Exposure time [s]	Ganymede diameter ["]	Spatial resolution [km/pix]
7939	O53K01010	1998-10-30	08:21:19	850.197	1.710	75.782
	O53K01020	1998-10-30	08:38:57	850.195	1.710	75.786
	O53K01030	1998-10-30	09:40:09	1205.200	1.709	75.799
	O53K01040	1998-10-30	10:07:22	1205.197	1.709	75.805
	O53K01050	1998-10-30	11:16:55	1125.199	1.709	75.821
	O53K01060	1998-10-30	11:42:48	1100.191	1.709	75.826
	O53K01070	1998-10-30	12:53:42	1200.199	1.708	75.842
	O53K01080	1998-10-30	13:17:10	1130.197	1.708	75.847
8224	O5D602010	2000-12-23	03:45:05	740.191	1.747	74.156
	O5D602020	2000-12-23	04:00:53	740.198	1.747	74.157
	O5D602030	2000-12-23	05:00:44	1100.199	1.747	74.158
	O5D602040	2000-12-23	05:26:17	1100.197	1.747	74.159
12244 (Visit 1)	OBJY03010	2010-11-19	20:24:36	798.182	1.637	79.161
	OBJY03020	2010-11-19	20:41:22	798.196	1.637	79.163
	OBJY03030	2010-11-19	21:45:33	1179.197	1.636	79.168
	OBJY03040	2010-11-19	22:12:25	1179.191	1.636	79.171
	OBJY03050	2010-11-19	23:21:24	1179.198	1.636	79.178
	OBJY03060	2010-11-19	23:48:16	1179.197	1.636	79.181
	OBJY03070	2010-11-20	00:57:16	1179.199	1.636	79.188
	OBJY03080	2010-11-20	01:24:08	1179.192	1.636	79.190
	OBJY03090	2010-11-20	02:33:07	1179.199	1.636	79.197
	OBJY030A0	2010-11-20	02:59:59	1179.198	1.636	79.200
12244 (Visit 2)	OBJY11010	2011-10-01	09:38:24	813.190	1.783	72.680
	OBJY11020	2011-10-01	09:55:25	813.200	1.783	72.677
	OBJY11030	2011-10-01	10:55:46	1194.198	1.783	72.667
	OBJY11040	2011-10-01	11:22:53	1194.199	1.783	72.662
12244 (Visit 3)	OBJYB1010	2011-10-01	12:47:53	813.196	1.783	72.648
	OBJYB1020	2011-10-01	13:04:54	813.198	1.783	72.645
	OBJYB1030	2011-10-01	14:07:24	1194.196	1.784	72.634
	OBJYB1040	2011-10-01	14:34:31	1194.198	1.784	72.630
	OBJYB1050	2011-10-01	15:43:53	1209.195	1.784	72.618
	OBJYB1060	2011-10-01	16:07:30	1209.199	1.784	72.614
13328 (Visit 1)	OCBUG1010	2014-01-23	17:08:09	885.197	1.701	76.155
	OCBUG1020	2014-01-23	17:26:21	885.199	1.701	76.155
13328 (Visit 2)	OCBUI1010	2014-01-23	21:53:47	885.185	1.701	76.154
	OCBUI1020	2014-01-23	22:11:57	885.196	1.701	76.154
13328 (Visit 3)	OCBUG2010	2014-01-27	12:00:37	885.195	1.692	76.566
	OCBUG2020	2014-01-27	12:18:48	885.199	1.692	76.569
13328 (Visit 4)	OCBUH3010	2014-02-25	04:34:59	885.199	1.581	81.957
	OCBUH3020	2014-02-25	04:53:10	885.198	1.581	81.962

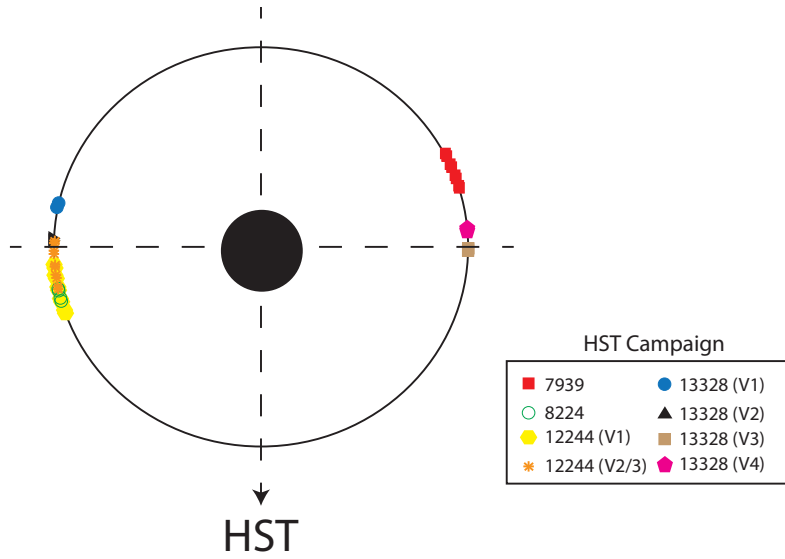


Figure 3.2: Orbital coverage of HST campaigns used in this thesis. The different visits are color-coded as indicated in the legend shown in the lower-right part of the figure.

In conclusion, the STIS images provide spectral and spatial information for different line emissions. The G140L grating operates in a wavelength range between 1150 and 1730 Å, allowing us to study the Lyman- α emission line ($\lambda = 1215.67\text{\AA}$). This observational setup has observed Jupiter's moon Ganymede at different occasions and with different observational characteristics, allowing the search for potential differences between the various visits.

Chapter 4

Image processing

In order to properly analyze the HST STIS images, it is important to process them to relate the detected counts to physical quantities. Section 3 dealt with the explanation of how the information is presented in the images. In this section, we explain the processing methods used for the proper analysis of the STIS images.

In order to increase the signal to noise ratio, we combine the individual datasets of each visit presented on Table 3.1. However, depending on the geometry of the observation, geocoronal emissions at Lyman- α vary between approximately 15 kR and 5 kR. In order to minimize this contribution, which obscures the signal from the moon, we identify and combine only the datasets in which the geocoronal emissions are lower than 10 kR (see Figure 4.1).

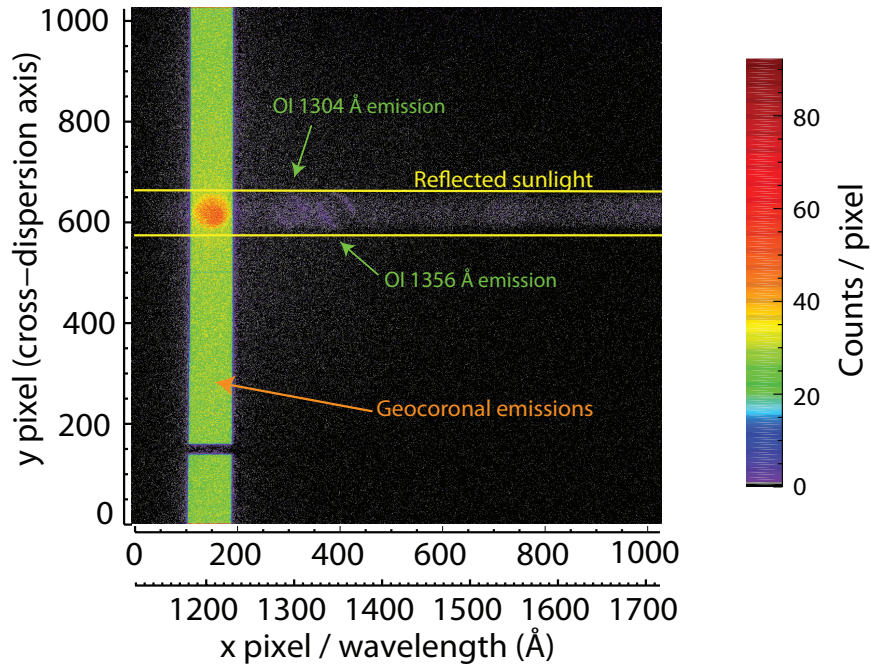


Figure 4.1: Combined HST STIS image from campaign 7939. The individual datasets with background emissions lower than 10 kR are combined. The trace of reflected sunlight (and oxygen aurora) can be observed along the x axis within the yellow lines. The geocoronal emission fills the entire slit at the hydrogen (1216 \AA) emission line.

Section 4.1 deals with the conversion from detected counts to brightness. In section 4.2 we explain how the STIS images are oriented, while in section 4.3 we explain the method to find

the exact position of Ganymede's disk within the Lyman- α slit.

4.1 Unit conversion

In order to make the signal observed in the STIS images comparable to physical quantities, we must perform a unit conversion. The arrays provided by the *flt* files have units of detector counts per pixel. The unit Rayleigh for brightness is often used in photometric studies, and it is defined as (Hunten et al., 1956):

$$1[\text{R}] = \frac{10^6}{4\pi} \left[\frac{\text{photons}}{\text{cm}^2 \text{ s sr}} \right]. \quad (4.1.1)$$

In order to relate the detector counts to the brightness observed in each pixel, one must consider the different factors that characterize the observation. The relation between the signal given in the *flt* files and the brightness is given by

$$B[\text{R}] = \frac{4\pi}{10^6} \cdot \frac{S}{T_{exp} \cdot A_{eff}(\lambda) \cdot \Omega} \quad (4.1.2)$$

where B stands for the photometric brightness in [R], S stands for the detector counts in [counts pix^{-1}], T_{exp} is the exposure time in [s], A_{eff} is the effective area of the telescope in [cm^2 counts photons^{-1}], Ω is the solid angle in [sr], and the term $4\pi \times 10^{-6}$ stands for the definition of the unit Rayleigh.

The exposure time T_{exp} is specified in the main header of the *flt* files. The solid angle covered by each pixel is given by

$$\Omega[\text{sr}] = m_{x_d} \cdot m_{y_d} \cdot \left(\frac{2\pi}{3600 \cdot 360} \right)^2 \quad (4.1.3)$$

where m_{x_d} and m_{y_d} are the plate scales of the detector in [arcsec] in the x and y directions, also specified in the header of the *flt* files, and the numerical term stands for the conversion from [arcsec^2] to [sr].

Finally, the effective area of the telescope is obtained by

$$A_{eff} = A \cdot T(\lambda) \quad (4.1.4)$$

where $A=45239$ [cm^2] is the area of the telescope, and $T(\lambda)$ is the wavelength-dependent throughput. The throughput is a property of the detector related to its sensitivity. It represents the fraction of the photons passing through the system, and thus being counted by the detector.

The throughput curve with respect to the wavelength, specific of the grating and aperture of the observations, is obtained from the calibration files, which are also specified in the header of the data files. As it is a wavelength dependent quantity, it must be applied taking into account the wavelength associated with each pixel in the x direction. However, all the pixels within the slit at Lyman- α will represent this wavelength, and thus a constant throughput must be applied within the slit. However, when analyzing the FUV albedo at different wavelengths, we include the wavelength-dependent sensitivity.

In conclusion, we have derived a relation between the counts detected by STIS to the brightness. Such a conversion allows for the comparison between the different HST Campaigns, as well as with the other Galilean moons.

4.2 Image orientation

The relative geometry between the moon and the detector in the observations is essential for understanding the physical processes occurring on Ganymede and its surroundings. In this section, we explain how the STIS image is oriented with respect to the moon’s body-fixed reference frame.

Figure 4.2 shows a sketch of the relevant directions regarding the orientation of the STIS image. In this sketch, as well as in the STIS images (see Figure 4.1), the detector y-axis points upwards. Due to a small tilt, the detector and aperture axes are not perfectly aligned, with a difference lower than 1.5° .

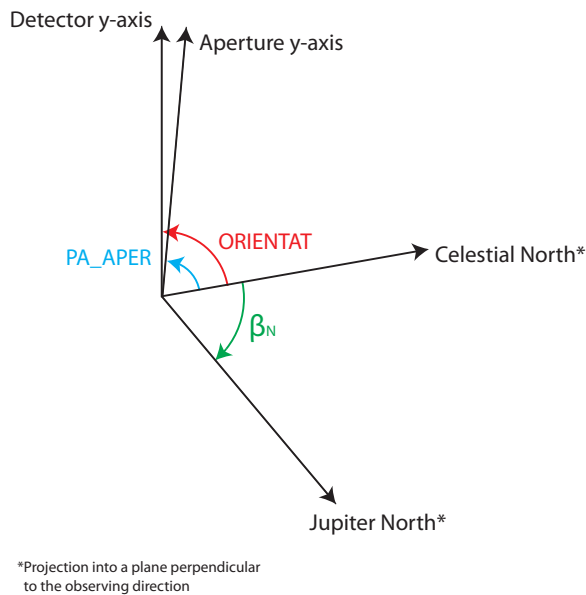


Figure 4.2: Sketch showing the relevant directions and angles for the orientation of the STIS images.

The angles *ORIENTAT* and *PA_APER* are both specified in the main header of the *flt* files. They represent the angles between the celestial north and the detector and aperture y-directions, respectively, defined as positive in the counterclockwise direction (Bostroem, 2010). We calculate the angle between the celestial north and Jupiter north as seen from the HST, β_N , using the SPICE toolkit provided by NAIF (<https://naif.jpl.nasa.gov/naif/toolkit.html>). Defining this angle as positive in the clockwise direction, the rotation θ_{rot} of the STIS images for the north of the moon to point up is given by

$$\theta_{rot} = \beta_N + ORIENTAT. \quad (4.2.1)$$

In order to check the correct calculation of the relevant angles, we obtain images of Ganymede at the oxygen line OI 1304Å. Figure 4.3 shows rotated images at 1216 and 1304 Å, with the Jovian north direction pointing upwards. The images at Lyman- α mainly represent reflected sunlight, and the identification of individual features is complicated. However, the auroral oxygen emissions allow us to identify bright spots and compare their location with previous studies (e.g. Feldman et al. (2000); Musacchio et al. (2017)).

In this study, we do not perform a rotation of the STIS images for the analysis of the data. However, understanding the orientation of the images is important, especially when modeling

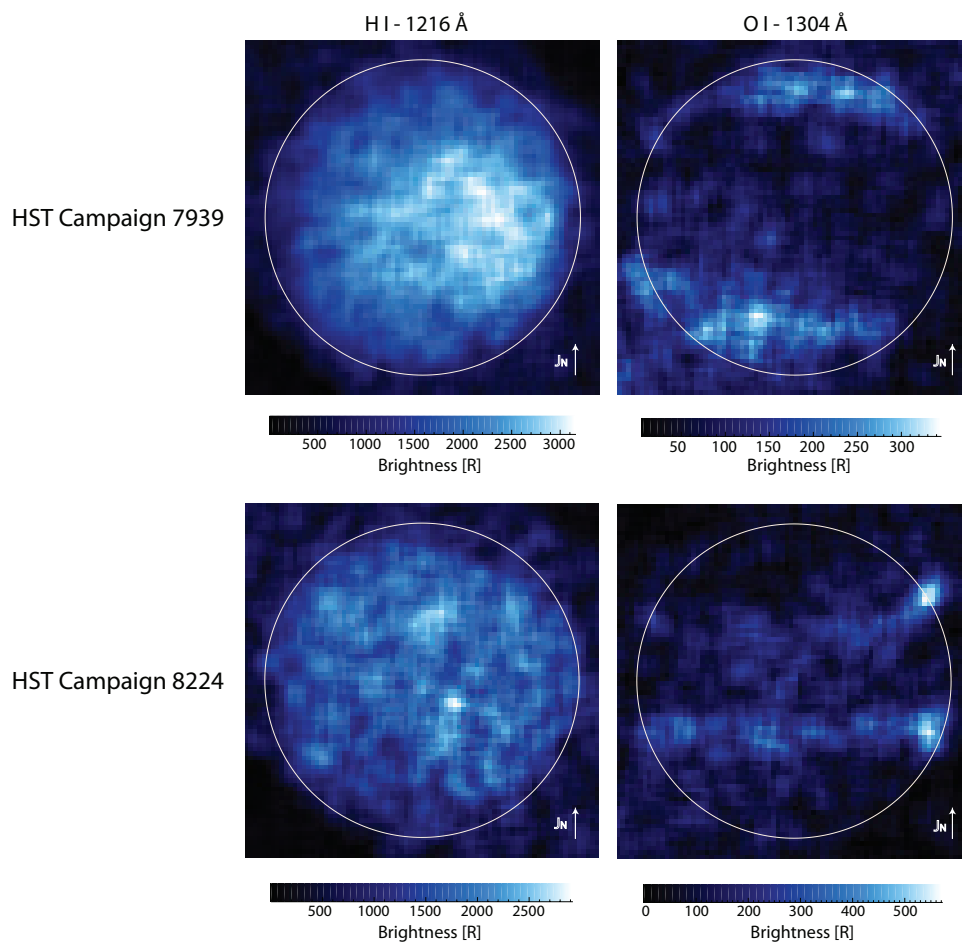


Figure 4.3: Smoothed STIS images at 1216 and 1304 Å for HST Campaigns 7939 and 8224. The STIS image is rotated for the direction of Jupiter north to point upwards.

the reflected sunlight in the moon’s surface in section 5.1, in which rotation of visible images is necessary for the correct estimation of the surface reflectivity.

4.3 Location of the disk

The location of Ganymede’s disk in the STIS images is not known in advance. Hence, a method for obtaining its position within the Lyman- α slit is required.

First of all, we perform a background subtraction to the STIS image within the Lyman- α slit. The background emission is estimated for each x value obtaining the mean value of the signal along pixels above and below the disk. Then, the background emission is subtracted from the initial STIS image.

We obtain solar spectral information measured by the SOLSTICE instrument on the UARS (Upper Atmosphere Research Satellite). The solar spectrum is convolved with a uniform disk with the same size as Ganymede’s disk appears in the STIS images. Then, this synthetic image is convolved with a point spread function (PSF) obtained from the Tiny Tim simulation software (Krist et al., 2011) (see section 5.1 for further explanation).

Figure 4.4 shows a sketch of the method used for locating Ganymede’s disk within the Lyman- α slit. Initially, the position of the moon is approximated. We multiply the pixels inside the disk in both the background-subtracted STIS image and the generated synthetic image, and we integrate over the whole disk. This process is repeated changing the location of the disk in the background-subtracted STIS image ± 10 pixels in each direction. A 20×20 array is obtained, with each pixel containing the integrated value for each location. We take the maximum value of the array as the best approximation for Ganymede’s position within the Lyman- α slit.

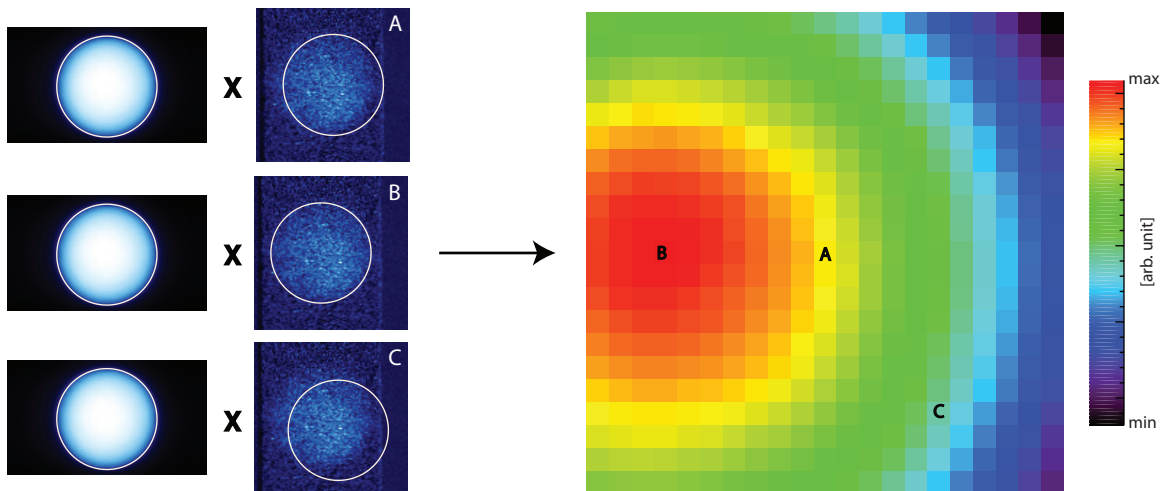


Figure 4.4: Sketch of the method used for obtaining the exact position of Ganymede’s disk within the Lyman- α slit for HST Campaign 7939.

Chapter 5

Image modeling

In this particular project, we are interested in the abundance of atomic hydrogen in Ganymede's atmosphere, and the study of the surface reflectivity at different wavelength ranges in the FUV. For the study of the hydrogen atmosphere, we analyze the Lyman- α wavelength. In the case of the study of the FUV reflectivity, we analyze the Lyman- α wavelength, and the trace of reflected sunlight between 1410 and 1700 Å.

For the modeling of the signal within the Lyman- α slit, we use the approach of Roth et al. (2017a), which considers four main sources of emission at this wavelength (see Figure 5.1): 1) Scattered light in the Earth's geocorona; 2) Scattered light at the interplanetary medium (IPM); 3) Reflected sunlight on Ganymede's surface; 4) Scattered light in Ganymede's atomic hydrogen corona. In the case of the signal between 1410 and 1700 Å, the analysis is simpler, as the signal is described only in terms of reflected sunlight and background noise.

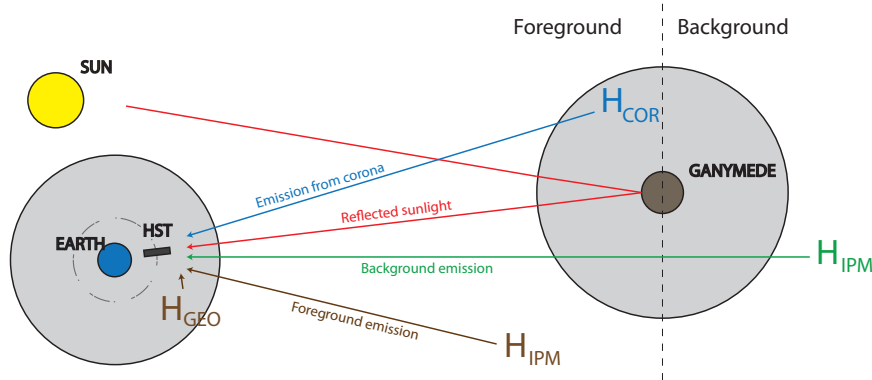


Figure 5.1: Not-to-scale sketch of the different contributions to the Lyman- α signal. The foreground emission stands for scattered light in the geocorona and in the IPM between Earth and Ganymede (brown). The solar flux is also scattered by the IPM behind Ganymede (green), which gives name to the background emission, and by Ganymede's hydrogen corona (blue). Additionally, the solar flux is reflected by the moon's icy surface (red).

We choose 1D profiles along the slit in the cross-dispersion axis, like the one shown in Figure 5.2, for the comparison between the images and model within the Lyman- α slit. The pixel brightness at this wavelength is given by

$$I_{mod_{Ly-\alpha}} = I_{fg} \cdot c_{fg} + I_{bg} \cdot e^{-\sigma_{IPM} N_H} + I_{disk} \cdot p_{Ly-\alpha} \cdot e^{-2\sigma_{SUN} N_H} + I_{corona} \quad (5.0.1)$$

where the first two terms represent the foreground and background emission respectively, as defined in Figure 5.1; the third term stands for the reflected sunlight inside the disk, being $p_{Ly-\alpha}$ the albedo at Lyman- α ; and the last term includes the contribution from the scattered light at Ganymede's hydrogen corona.

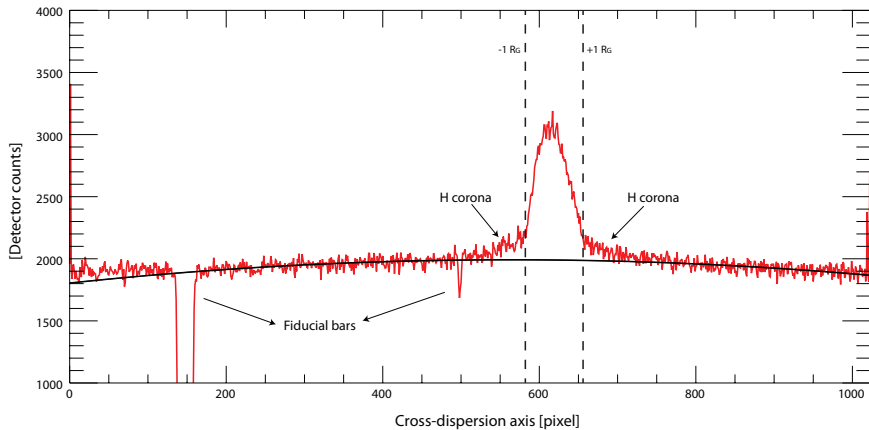


Figure 5.2: Profile obtained by summing over 70 pixels (Ganymede diameter) along the x direction, centered at the center of the disk at Lyman- α , for the STIS campaign 7939. The dashed lines show the edges of the moon's disk. Signal decreasing towards the sides of the disk indicate the presence of atmospheric emissions.

The exponential functions in the second and third terms represent the extinction of the solar flux and the IPM background in Ganymede's hydrogen corona. The quantities σ_{IPM} and σ_{SUN} stand for the effective cross sections, which are estimated in Appendix A.1 using a radiative transfer model, taking into account the relevant line profiles and Doppler shifts.

We also estimate the extinction of the emission from Ganymede's hydrogen corona in the Earth's upper atmosphere (see Appendix A.2). This extinction is not included in the model, but our estimations suggest that the effect can be important for some of the HST campaigns. Its implications are further discussed in section 7.

In the case of the signal observed in the wavelength range between 1410 and 1700 Å, the brightness in each pixel is modeled by

$$I_{mod\lambda} = I_{bg} + I_{disk} \cdot p_{\lambda} \quad (5.0.2)$$

where I_{bg} stands for the background noise, and the second term represents the reflected sunlight.

The following sections deal with the derivation and explanation of the models for each of the terms in equation 5.0.1. Then, the comparison between the model and the real profiles leads to the results evaluated in section 6, which also deals with the analysis of the wavelength range 1410-1700 Å. Finally, the results of the study are discussed in Section 7.

5.1 Model for the reflected sunlight

The trace of solar reflected emission from Ganymede's disk can be directly observed in the STIS images along the x direction, as shown in Figure 4.1. In order to understand the Lyman- α emission wavelength, it is important to quantify the contribution from the reflected sunlight

at the moon's surface. This section deals with the modeling procedure for that specific source of emission.

First of all, solar spectral information taken with the SOLSTICE instrument on UARS is obtained from the LASP (Laboratory for Atmospheric and Space Physics) web site (<http://lasp.colorado.edu/home/solstice/data/>). The SOLSTICE instrument provides daily solar UV spectra with a spectral resolution of 1 nm, and normalized to 1 AU. Additionally, it also provides high-spectral-resolution data (0.05 nm) for periods of high, medium, and low solar activity. For this study, we use high-resolution spectra and scale it to the composite Lyman- α flux at the dates in which Ganymede was observed by the HST.

The composite Lyman- α flux adopted for the scaling factor of the solar spectrum must be corrected for solar rotation. This correction stands for the variations in the solar emission due to the rotation of the Sun. Taking into account that the measurements of the solar flux are made in the Earth's vicinity, the time-shift between the positions of Ganymede and the Earth with respect to the Sun is calculated, accounting for the difference in the solar longitude between both bodies. Then, the corrected composite Lyman- α can be determined.

The scaled solar spectrum gives us information about the incident solar flux at Ganymede. However, the observed magnitude in the HST/STIS images is the reflected sunlight, which will depend on different factors, like the properties of the surface reflectivity, or the illumination characteristics. Sections 5.1.1 and 5.1.2 explain how these features are modeled. Then, section 5.1.3 explains how we include the different properties into a 2D image comparable to the STIS images.

5.1.1 Surface reflectivity at Lyman- α

The model for the reflected sunlight must take into account the properties of Ganymede's surface reflectivity at the Lyman- α wavelength. However, the reflectivity of the moon at this wavelength is not fully known.

Images of Europa (McGrath et al., 2009; Roth et al., 2014) suggest an anti-correlation between the surface reflectivity at Lyman- α and visible wavelengths. This behavior has also been observed in the Moon (Seifert et al., 2014), and thought to be related with space weathering processes, although it is still not fully understood if that is the cause of the inversion of Europa's surface reflectivity.

The spectral inversion of the reflectivity in the FUV is supported by the geometric albedo values reported in previous studies of Ganymede (Hendrix et al., 2005; Hall et al., 1998; Nelson et al., 1987; Musacchio et al., 2017). Figure 5.3 shows the observed UV albedos as a function of wavelength, for both the trailing and leading hemispheres. Figure 5.4 shows the reflectance rotational curve for different wavelengths. These figures tell us that the leading hemisphere is brighter than the trailing in the NUV and MUV, which is also true for the visible range (Pappalardo et al., 2004). However, while looking at shorter wavelengths, the rotational curve of Ganymede starts to flatten, and the reflectances of both hemispheres become more similar. At some wavelength in a range between 1500-2000 Å, the trailing side turns to be brighter than the leading hemisphere, suggesting the spectral inversion of Ganymede's surface reflectivity. Therefore, at the Lyman- α wavelength, we expect the trailing hemisphere to be brighter, and therefore anti-correlated with the reflectivity at visible wavelengths.

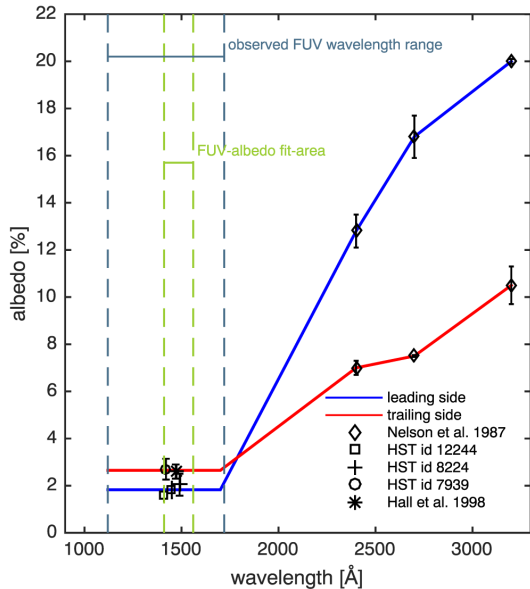


Figure 5.3: *Ganymede's hemispherical albedo versus wavelength from Musacchio et al. (2017). The leading hemisphere is brighter in the MUV, but darker in the FUV.*

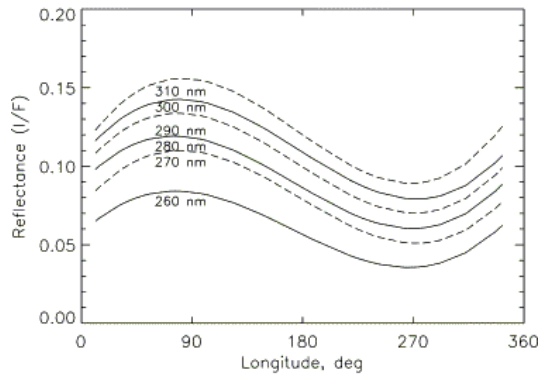


Figure 5.4: *Rotational phase curve of Ganymede from Hendrix et al. (2005). Longitudes from 0 to 90 represent the leading hemisphere, while from 180 to 360 they represent the trailing hemisphere.*

Hence, for generating the model for the reflected sunlight, we invert visible images of Ganymede. The geometry of the observations is taken into account by using the SPICE-enhanced version of Cosmographia, which is a visualization tool of the Solar System developed by NAIF (<https://naif.jpl.nasa.gov/naif/cosmographia.html>). Then, the images are properly rotated, as explained in section 4.2, to match the orientation of the STIS images.

As explained in section 4, the different datasets of each observation are summed up in order to increase the signal-to-noise ratio. Therefore, in the STIS images we use, the region of the moon's surface facing the HST changes due to the rotation of the moon around its own axis. In order to take into account this effect in the modeled surface reflectivity, different visible images during the whole exposure are obtained with Cosmographia, and then added to each other.

The anti-correlation of the surface reflectivity at visible wavelengths and at Lyman- α is a material-dependent feature. This means that the reflectivity at different regions of the moon could be related differently between Lyman- α and visible wavelengths. Thus, how the inversion of the images should be performed is not fully known. In order to take into account different possible scenarios for the surface reflectivity, we consider five different approaches regarding the inversion of the visible images. Approaches 1-4 (see Figure 5.5) consider inverted visible images, with different definitions for the inversion. We also consider Approach 5, which is the limit case in which the reflected sunlight is modeled as a uniformly reflecting disk.

The inversion of the images is performed by subtracting the mean value of the pixels within the disk to each pixel of the visible image, obtaining the residual value. Then, the residuals are subtracted from a homogeneous disk, obtaining the inverted visible image. The different brightnesses considered for the homogeneous disk lead to the different definitions of the inversion, as shown in Figure 5.5. Mathematically, the inverted visible images are

described by:

$$B_{inv}(x, y) = \begin{cases} 2\hat{B} - B(x, y) & \rightarrow \text{Approach 1} \\ 4\hat{B} - B(x, y) & \rightarrow \text{Approach 2} \\ 6\hat{B} - B(x, y) & \rightarrow \text{Approach 3} \\ 8\hat{B} - B(x, y) & \rightarrow \text{Approach 4} \end{cases}$$

where \hat{B} is the mean value of the visible image, and $B(x, y)$ is the value of each pixel. Finally, the resolution of the image is decreased to match the resolution of the STIS images (see Table 3.1), and it is normalized for an average pixel to have a unit value.

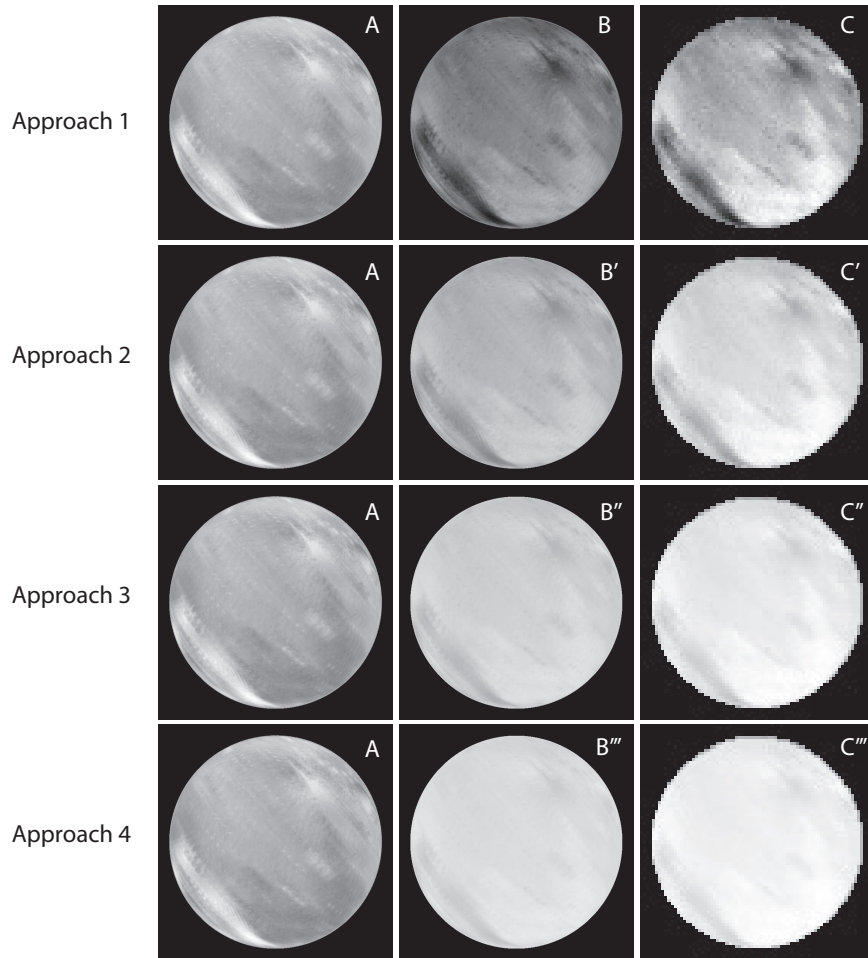


Figure 5.5: Inversion of the visible images used for constructing the reflected sunlight model for the HST campaign 1979. The visible image with the STIS orientation (A) is inverted using different approaches (B-B'''). Finally, the resolution of the images is decreased (C-C''').

In conclusion, we have created a model to take into account the reflectivity of Ganymede's surface. The observed albedo values and other studies of Europa suggest an anti-correlation between the surface reflectivity at Lyman- α and visible wavelengths. Our model considers five different approaches with different inversions of visible images of Ganymede, in order to take into account different scenarios for the inversion, as the physics of this phenomenon are still not fully understood.

5.1.2 Illumination phase functions

As explained in the beginning of section 5.1, the only known parameter regarding the reflected sunlight is the observed solar flux at 1 AU. Hence, it is necessary to relate this quantity to the reflected sunlight in Ganymede observed by the HST. The relation between the solar flux at 1 AU and the observed reflected sunlight is derived by Karttunen et al. (2007), and given by

$$F_G(\lambda) = F_\odot(\lambda) \cdot p \cdot \phi(\alpha) \cdot \frac{a^2 R_G^2}{\Delta^2 r^2}, \quad (5.1.1)$$

where F_G is the observed reflected solar flux at Ganymede's surface; F_\odot is the solar flux at 1 AU; p is the geometric albedo; $\phi(\alpha)$ is the phase function, which gives the dependence with solar phase angle, defined as the angular distance between the Sun and the Earth at Ganymede; a is the distance $a = 1$ AU; R_G is Ganymede's radius; Δ is the distance between the Earth and Ganymede; and r is the distance between the Sun and Ganymede.

In order to model the reflection of the solar flux on Ganymede's surface, we include three different phase functions for estimating the latitudinal and longitudinal dependencies of the reflectance:

- The first approach considers a uniform phase function, or in other words, considers no dependence of the observed flux with the solar incident angle and the observing geometry. Mathematically, this is expressed as

$$\phi(\theta_i, \theta_r) = 1. \quad (5.1.2)$$

- The second approach considers a Lambertian surface. This model suggests that the apparent brightness of the surface to the observer is the same, regardless of the observing direction. Thus, the dependence is just a function of the incident angle θ_i , as defined in Figure 5.6. The phase function of a Lambertian surface is given by

$$\phi(\theta_i, \theta_r) = \begin{cases} \cos(\theta_i) & \text{if } 0 \leq \theta_i \leq \pi/2 \\ 0 & \text{if } \theta_i > \pi/2 \end{cases} \quad (5.1.3)$$

- The third approach considers the reflectance model derived by Oren and Nayar (1994). This model considers the incident and observing directions, with the definitions of the different angles as given in Figure 5.6. Besides, it also considers the roughness of the surface. The phase function is given by

$$\begin{aligned} \phi(\theta_i, \theta_r) = & \cos(\theta_i) \cdot [C_1 + C_2 \cdot \cos(\phi_r - \phi_i) \cdot \tan(\beta) \\ & + C_3 \cdot (1 - \cos(\phi_r - \phi_i) \cdot \tan\left(\frac{\alpha + \beta}{2}\right)), \end{aligned} \quad (5.1.4)$$

where $\alpha = \text{Max}(\theta_r, \theta_i)$, $\beta = \text{Min}(\theta_r, \theta_i)$ and the factors C_1, C_2 and C_3 are given by

$$C_1 = 1 - 0.5 \frac{\sigma^2}{\sigma^2 + 0.33},$$

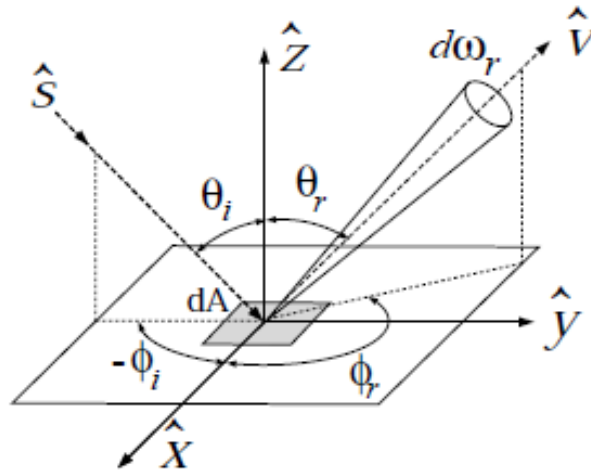


Figure 5.6: Geometric definitions for the incident and observing angles from Oren and Nayar (1994). The \hat{Z} direction is coincident with the normal direction to the surface.

$$C_2 = \begin{cases} 0.45 \frac{\sigma^2}{\sigma^2 + 0.09} \sin(\alpha) & \text{if } \cos(\phi_r - \phi_i) \geq 0 \\ 0.45 \frac{\sigma^2}{\sigma^2 + 0.09} \left(\sin \alpha - \left(\frac{2\beta}{\pi} \right)^3 \right) & \text{otherwise} \end{cases},$$

$$C_3 = 0.125 \left(\frac{\sigma^2}{\sigma^2 + 0.09} \right) \left(\frac{4\alpha\beta}{\pi^2} \right)^2.$$

The parameter σ represents the roughness of the surface. Note that when $\sigma = 0^\circ$, the model reduces to the Lambertian case in equation 5.1.3.

In principle, the roughness parameter σ is unknown. Photometric studies of Ganymede (Buratti, 1991; Domingue and Verbiscer, 1997) suggest that the roughness parameter, as defined for Hapke's reflectance model (Hapke, 2012), is approximately 30° . We use a roughness parameter $\sigma = 30^\circ$ as an approximation.

Figure 5.7 shows an example of the three different phase functions considered in our model for the reflected sunlight, as described by equations 5.1.2, 5.1.3 and 5.1.4. The reflectance model derived by Oren and Nayar (1994) represents a case inbetween the Lambertian and uniform approaches.

In conclusion, apart from including the properties of Ganymede's surface reflectivity in our model, we also include different phase functions in order to take into account the illumination and observing characteristics. These phase functions will be applied to each of the different approaches describing the reflectivity of the moon's surface.

5.1.3 Spatial-spectral setup of STIS images

Sections 5.1.1 and 5.1.2 have dealt with the description and modeling of Ganymede's surface reflectivity and the phase functions. In this section, we will focus on how we include the

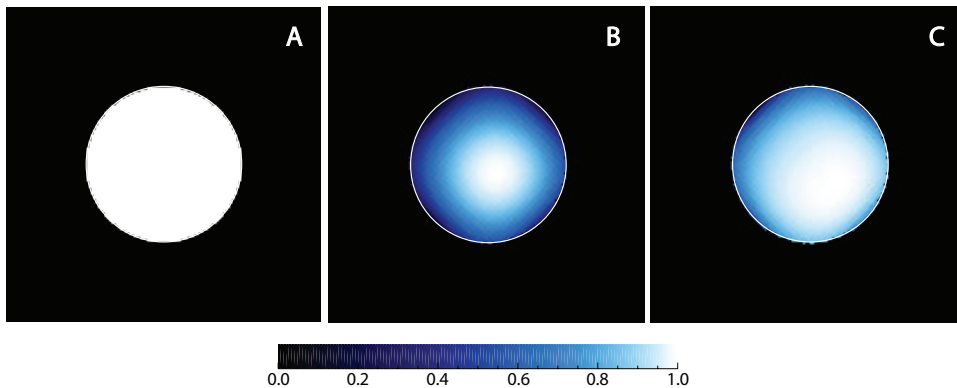


Figure 5.7: Phase functions computed for HST Campaign 7939. A) Uniform phase function, as equation 5.1.2. B) Phase function for a Lambertian surface, described by equation 5.1.3. C) Phase function from the reflectance model of Oren and Nayar (1994), assuming a roughness parameter of 30° .

different characteristics of the reflected sunlight into a 2D image comparable to the HST/STIS images.

The solar spectrum corrected for solar rotation introduced in section 5.1 must be converted into a 2D image. First of all, it is necessary to calculate the brightness per pixel, so a unit conversion from flux to brightness per pixel in Rayleigh [R] is performed:

$$I[R] = \frac{F(\lambda_d)}{m_{x_d} \cdot m_{y_d}} \cdot \Delta\lambda \cdot \left(\frac{3600 \cdot 360}{2\pi} \right)^2 \cdot \frac{4\pi}{10^6} \quad (5.1.5)$$

where $F(\lambda_d)$ is the presented spectral photon flux in [photons/cm²/s/Å]; m_{x_d} and m_{y_d} are the plate scales of the detector in each direction, given in [arcsec]; $\Delta\lambda$ is the dispersion coefficient, which is 0.584 [Å pixel⁻¹] for the STIS G140L grating; the last two terms stand for unit conversion from [arcsec²] to [ster] and the definition of Rayleigh.

Then, the solar spectral brightness is convolved with a disk of the same size as the moon. This disk must represent different features of the reflected sunlight, like the different reflectivity at different regions of the surface, or the illumination characteristics. Hence, we convolve the solar spectral brightness with the 5 different approaches for the surface reflectivity (see Figure 5.8). Then, the three modeled phase functions are applied to each of the different approaches, giving rise to 15 different images, as shown in Figure 5.9.

The synthetic 2D images created for the solar emission are then convolved with a point spread function (PSF) in order to take into account the imaging response of the detector. For our model, we use the Tiny Tim simulation software (Krist et al., 2011), which generates simulated PSFs for the different instruments on the HST.

It must be noted that the albedo p in equation 5.1.1 is not known. Musacchio et al. (2017) reported values for the albedo of approximately $2.7 \pm 0.4\%$ for the trailing hemisphere, and $1.8 \pm 0.4\%$ for the leading side in the wavelength range 1410-1550 Å. However, the albedo is a wavelength-dependent quantity, indicating that the reflectivity of the surface at Lyman- α might not be equal to the one in the 1410-1550 Å range. Thus, the model created for the reflected sunlight can be linearly scaled with the albedo at Lyman- α $p_{Ly-\alpha}$ in equation 5.0.1.

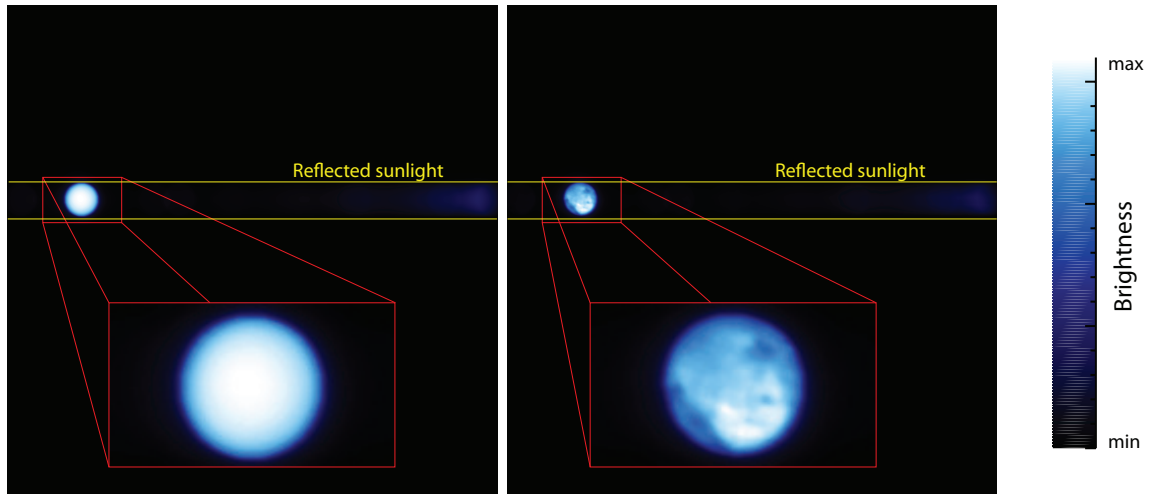


Figure 5.8: Examples of synthetic 2D images created for HST Campaign 7939, corresponding to Approaches 5 (left) and 1 (right), with a uniform phase function. The region between the two yellow lines represents the trace of reflected sunlight along the spectrum, which is comparable to the STIS image in Figure 4.1. The red box represents a zoom of the image at Lyman- α , which is much brighter than the rest of the spectrum. At this particular wavelength the difference between the two approaches is clear.

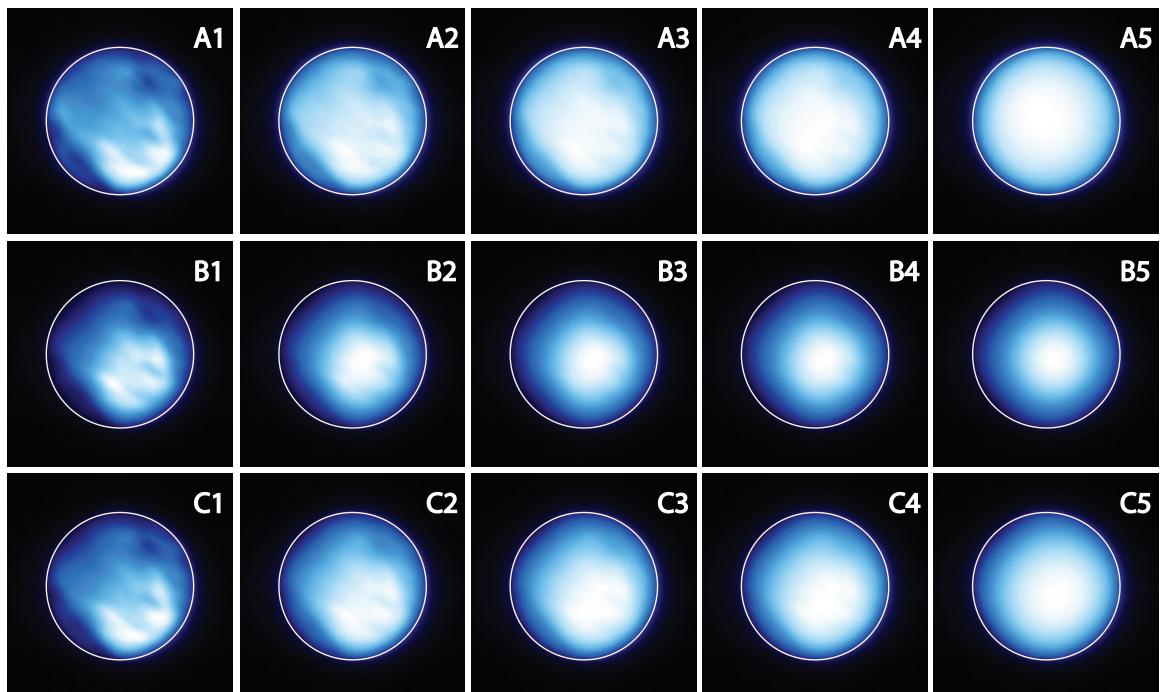


Figure 5.9: Synthetic 2D images created for HST Campaign 7939, with the moon centered at Lyman- α . The letters A-C correspond to the different phase functions in Figure 5.7. The numbers 1-4 correspond to the different definitions in the inversion of the inverted visible images shown in Figure 5.5, and number 5 corresponding to the case of uniform reflectivity.

5.2 Model for the scattered light at Ganymede's H corona

Although the composition of Ganymede's surface is not fully known, it appears to be mostly covered by water-ice (Spencer, 1987). For this reason, it is assumed that the main sources of Ganymede's atmosphere are the sublimation and sputtering of water-ice, together with the sputtering of OH, H₂, O₂ and H (Marconi, 2007).

Hence, atomic hydrogen can be created directly from the sputtering of the surface. However, the atmospheric model derived by Marconi (2007) suggest that the main sources of H are the dissociation of H₂O and H₂. H₂O is produced by the sublimation and sputtering of the surface. Their model suggest that the sublimation component is more important, and the abundance of H₂O turns out to be greater near the subsolar point, as it is observed in Figure 5.10. On the other hand, H₂ is mostly created by sputtering from magnetospheric particles, which occurs in regions close to the poles, where the magnetic field lines of Ganymede's magnetosphere are open. Thus, atomic hydrogen created by dissociation of H₂O by either UV photons or electron impact seems to be more important in regions near the subsolar point, while at higher latitudes dissociation of H₂ seems to be the main source of atmospheric H.

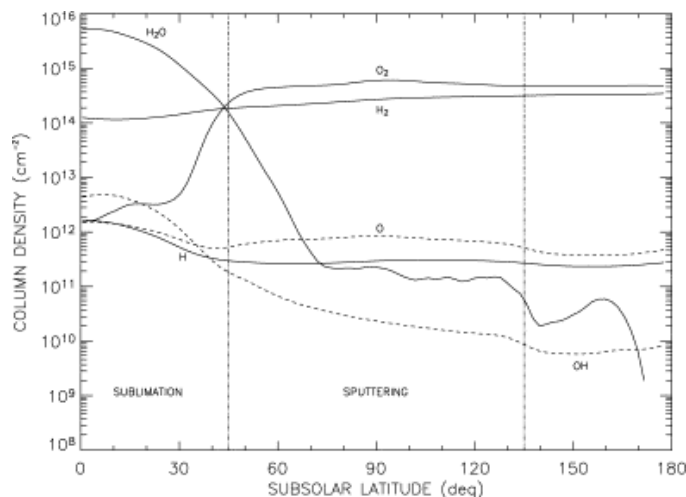


Figure 5.10: Radial column density as a function of subsolar latitude, from Marconi (2007). Sputtering of the surface is considered to be dominant in the polar regions (45°-135°), whereas sublimation is more important near the subsolar point (0°-45°)

Therefore, latitudinal and longitudinal variations in the abundance of atomic hydrogen are expected. However, we expect these variations to become homogeneous due to the high speed and temperatures of hydrogen atoms ($T_H \approx 1000$ K) (Marconi, 2007). For this reason, we assume a radially symmetric corona.

The next step consists in deriving a density distribution for hydrogen. Assuming a constant temperature of $T_H = 1000$ K, the most probable velocity of hydrogen atoms is $v_{th} = \sqrt{2k_B T_H / m_H} = 4.06$ km/s. Given that Ganymede's escape velocity is $v_{esc} = 2.74$ km/s, the escape parameter is $\lambda_{esc} = (v_{esc} / v_{th})^2 = 0.46$, which implies that hydrogen atoms are allowed to escape (Johnson et al., 2008).

Assuming a radially symmetric escaping corona, the density distribution (see Appendix B.1) is given by

$$n(r) = n_0 \left(\frac{R_G}{r} \right)^2, \quad (5.2.1)$$

where n_0 is the number density at the surface, R_G is the radius of Ganymede, and r is the distance to the center of the moon. Such a distribution has been used in different approaches to study the abundance of atomic hydrogen in the Galilean moons (Barth et al., 1997; Roth et al., 2017b,a).

Once the density distribution is determined, the line-of-sight column density can be calculated taking into account the geometry of the observations (see Appendix B.2), and is given by

$$N(r) = \begin{cases} n_0 \frac{R_G^2}{r} \arcsin\left(\frac{r}{R_G}\right) & \text{if } r \leq R_G \\ n_0 \frac{R_G^2}{r} \pi & \text{if } r > R_G \end{cases} \quad (5.2.2)$$

The photon scattering coefficient (or g -factor) allows for the calculation of resonantly scattered light in all directions. The definition of the g -factor is given by Chamberlain and Hunten (1987) as

$$g = \pi F_{\lambda_0} \cdot \frac{\pi e^2}{m_e c} \cdot f \cdot \frac{\lambda_0^2}{c}, \quad (5.2.3)$$

where πF_{λ_0} is the line centre solar irradiance at Ganymede in [photon $\text{cm}^{-2} \text{s}^{-1} \text{\AA}^{-1}$], e is the electron charge, m_e is the mass of the electron, c is the speed of light, f is the oscillator strength ($f=0.416$ for Lyman- α) and λ_0 is the central wavelength at Lyman- α .

We calculate the conversion between the composite Lyman- α and the line center solar irradiance using the approach of Emerich et al. (2005), given by

$$\frac{f}{10^{11} \text{ cm}^{-2} \text{ s}^{-1} \text{\AA}^{-1}} = 0.64 \left(\frac{F}{10^{11} \text{ cm}^{-2} \text{ s}^{-1}} \right)^{1.21}. \quad (5.2.4)$$

The values of the photon scattering coefficients for the different observations are presented in Table 5.1. Then, the brightness per pixel for the resonantly scattered light at Ganymede's hydrogen corona is given by

$$I_{corona}[R] = 10^{-6} \cdot g \cdot N_H \quad (5.2.5)$$

where the factor 10^{-6} stands for the conversion to the unit Rayleigh.

The model created for the radially escaping corona (equation 5.2.5) allows to create a 2D image comparable to the STIS images (see Figure 5.11). The model image is then convolved with the same PSF as in section 5.1. It must be noted that although the model is generated in the entire image, it is only valid within the Lyman- α slit.

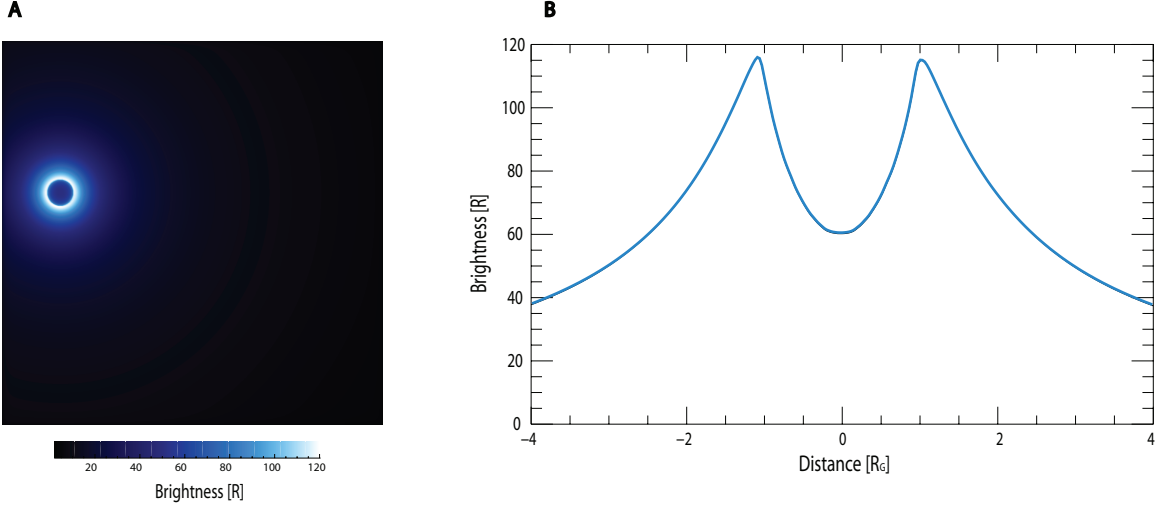


Figure 5.11: A) Synthetic 2D image of the model for a radially symmetric escaping hydrogen corona for the HST campaign 7939, assuming a surface density of $n_0=4 \times 10^3 \text{ cm}^{-3}$. The coordinates are transformed such that $r=0$ coincides with the center of the moon within the Lyman- α slit. B) Profile obtained by summing over $2R_G$ pixels in the x axis with centered at $r=0$.

Table 5.1: Composite Lyman- α at 1 AU, corrected for the solar longitude difference between Ganymede and the Earth; photon scattering coefficient; background emission from Pryor et al. (2008); and foreground emission.

HST Campaign ID	Composite Lyman- α [photons $\text{cm}^{-2} \text{ s}^{-1}$]	g -factor [photons s^{-1}]	Background emission [kR]	Foreground emission [kR]
7939	4.55×10^{11}	8.85×10^{-5}	0.44	3.64
8224	5.94×10^{11}	1.18×10^{-4}	0.31	4.19
12244 (V1)	3.86×10^{11}	7.29×10^{-5}	0.36	1.91
12244 (V2)	4.54×10^{11}	8.84×10^{-5}	0.39	2.82
12244 (V3)	4.54×10^{11}	8.85×10^{-5}	0.39	2.57
13328 (V1)	4.95×10^{11}	8.92×10^{-5}	0.33	4.37
13328 (V2)	4.95×10^{11}	8.93×10^{-5}	0.33	4.16
13328 (V3)	4.74×10^{11}	8.47×10^{-5}	0.31	4.83
13328 (V4)	5.11×10^{11}	9.24×10^{-5}	0.36	4.64

5.3 Model for the foreground and background emissions

The foreground and background contributions are the last terms of equation 5.0.1 to be modeled. These contributions are present along the whole slit at Lyman- α , and can be understood as an offset of the signal.

The background emission is caused by the scattered light in the IPM between Ganymede and infinity, as seen from the observer (see Figure 5.1). This contribution is not expected to vary along the slit, so it is considered constant. However, the background emission will be blocked by the moon's disk, and considering a constant contribution from the IPM along the whole slit makes us overestimate the contribution from this source at the disk. Hence, we consider this source to be zero at the disk and constant outside it. The brightness from the background emission is calculated using the single scattering model of Pryor et al. (2008). The expected contribution from this source for the different HST campaigns is presented in Table 5.1.

On the other hand, the scattered light at the Earth's geocorona and IPM between the Earth and Ganymede will be present along the whole slit, and not blocked by the moon's disk. This contribution is modeled by fitting a second order polynomial in regions where emissions from Ganymede's hydrogen corona are expected to be low (see Figure 5.12).

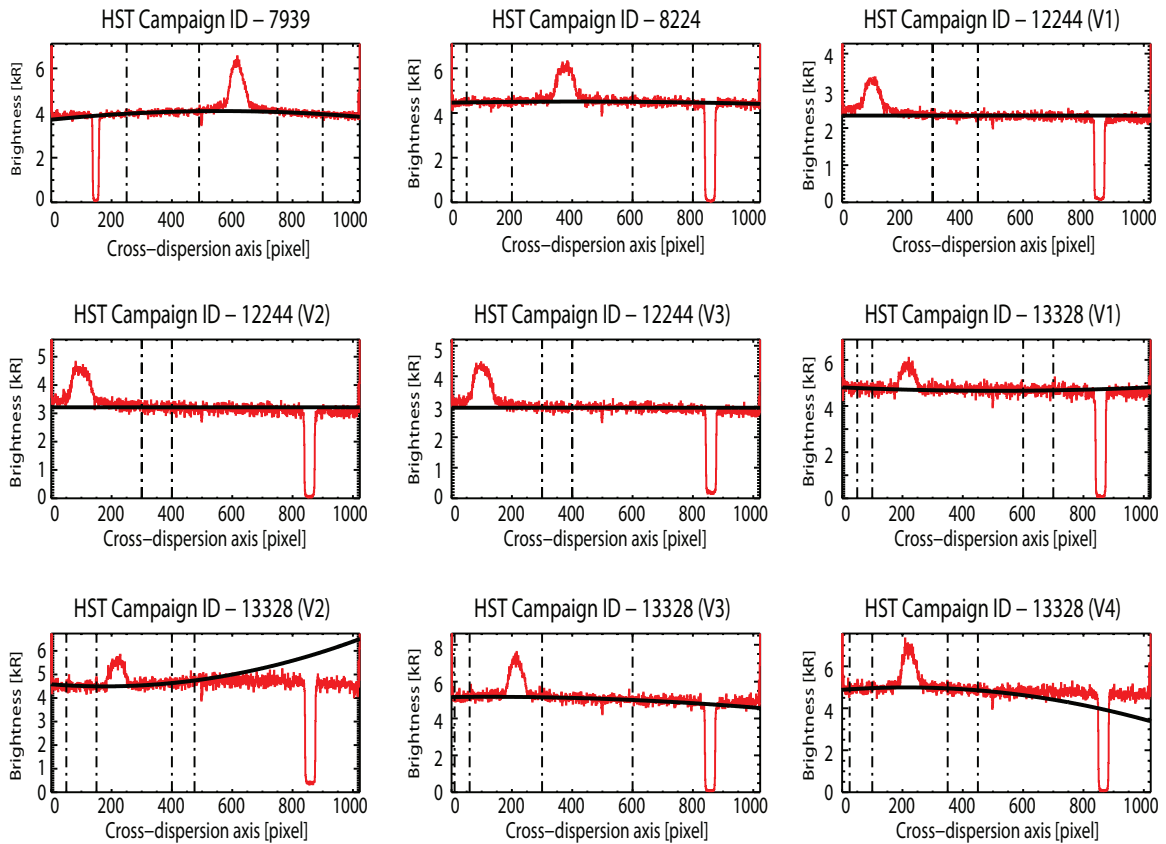


Figure 5.12: Foreground estimation for the different HST Campaigns. The red line corresponds to the STIS profile obtained by summing over Ganymede's diameter in pixels along the x axis, centered at the disk at Lyman- α . The black line is the second order polynomial fitted in the regions between the dashed lines, and used for estimating the foreground emission.

However, we must include the scaling factor c_{fg} for taking into account the presence of background emissions in the "foreground-fitting regions" presented in Figure 5.12. Although the contributions from scattered light in Ganymede's hydrogen corona are expected to be low at regions far from the moon, there must be included in the correcting factor, as the extent in which they contribute is not known in advance. Taking into account these contributions, we calculate a scaling factor $c_{fg_0}(y_i)$ at each y_i pixel within the "foreground-fitting regions", which is given by

$$c_{fg_0}(y_i) = \frac{I_{fg}(y_i) - I_{bg}(y_i) - I_{cor}(y_i)}{I_{fg}(y_i)}, \quad (5.3.1)$$

where I_{fg} represents the fitted profile in Figure 5.12, I_{bg} is the contribution from the background emissions, and I_{cor} is the emission from Ganymede's hydrogen corona. Then, we calculate the global scaling factor c_{fg} obtaining the mean value of all $c_{fg_0}(y_i)$.

In conclusion, the offset in the chosen profiles at Lyman- α (see Figure 5.12) with respect to zero emission outside the moon is mainly produced by the contributions from the foreground and background emissions. These contributions have been properly separated and modeled in order to avoid an overestimation of the the signal inside the moon's disk.

Chapter 6

Results

The comparison between the models and the images let us determine the contribution from the reflected sunlight and the scattered light in Ganymede's atomic hydrogen corona.

For the comparison between the model and images, we choose profiles in the cross-dispersion axis, summed over $2R_G$ pixels in the x direction, centered at the moon within the Lyman- α slit, like the ones shown in Figures 5.2 and 5.12. For each of the observations, we fit the model considering the 15 different approaches for the reflected sunlight presented in section 5.1. Besides, we consider two different cases: the first approach fits the model to the STIS profiles setting the contribution from the corona to zero, in which the only fit parameter is the albedo at Lyman- α $p_{Ly-\alpha}$. In the second case we introduce the contribution from the hydrogen corona, fitting in this case both the albedo $p_{Ly-\alpha}$ and the atomic hydrogen surface density n_0 .

Figure 6.1 shows the result from the fitting procedure for each of the approaches of the reflected sunlight, for HST campaign 7939. The reduced chi-squared values from the different approaches suggest that multiple models are in good agreement with the experimental profile. The difference between the derived surface density between the approaches corresponds to a systematic uncertainty that we include in the results presented in Table 6.1.

Nevertheless, when looking at the overall analysis of all HST campaigns, we find that the approach for the reflected sunlight that is in good agreement with all the observations is when using the second approach for the inverted visible images and the reflectance model of Oren and Nayar (1994) (C2 in Figures 6.1 and 5.9). Therefore, we present the results obtained with this particular approach, but including a systematic uncertainty.

Figure 6.2 shows the comparison between the model and the STIS profiles for each of the observations, when applying the chosen approach. Table 6.1 shows the numerical results obtained for the hydrogen corona in each of the campaigns. Besides, we include the extinction of the emission from Ganymede's hydrogen corona in the Earth's upper atmosphere, as estimated in Appendix A.2. Finally, Figure 6.3 shows the dependence of the atomic hydrogen surface density as a function of orbital longitude.

Regarding the study of the albedo, it must be noted that the geometric albedo at Lyman- α cannot be directly calculated from the fitting procedure, as the term I_{disk} of each pixel in equation 5.0.1 depends on how the inversion of the images is defined. After the surface

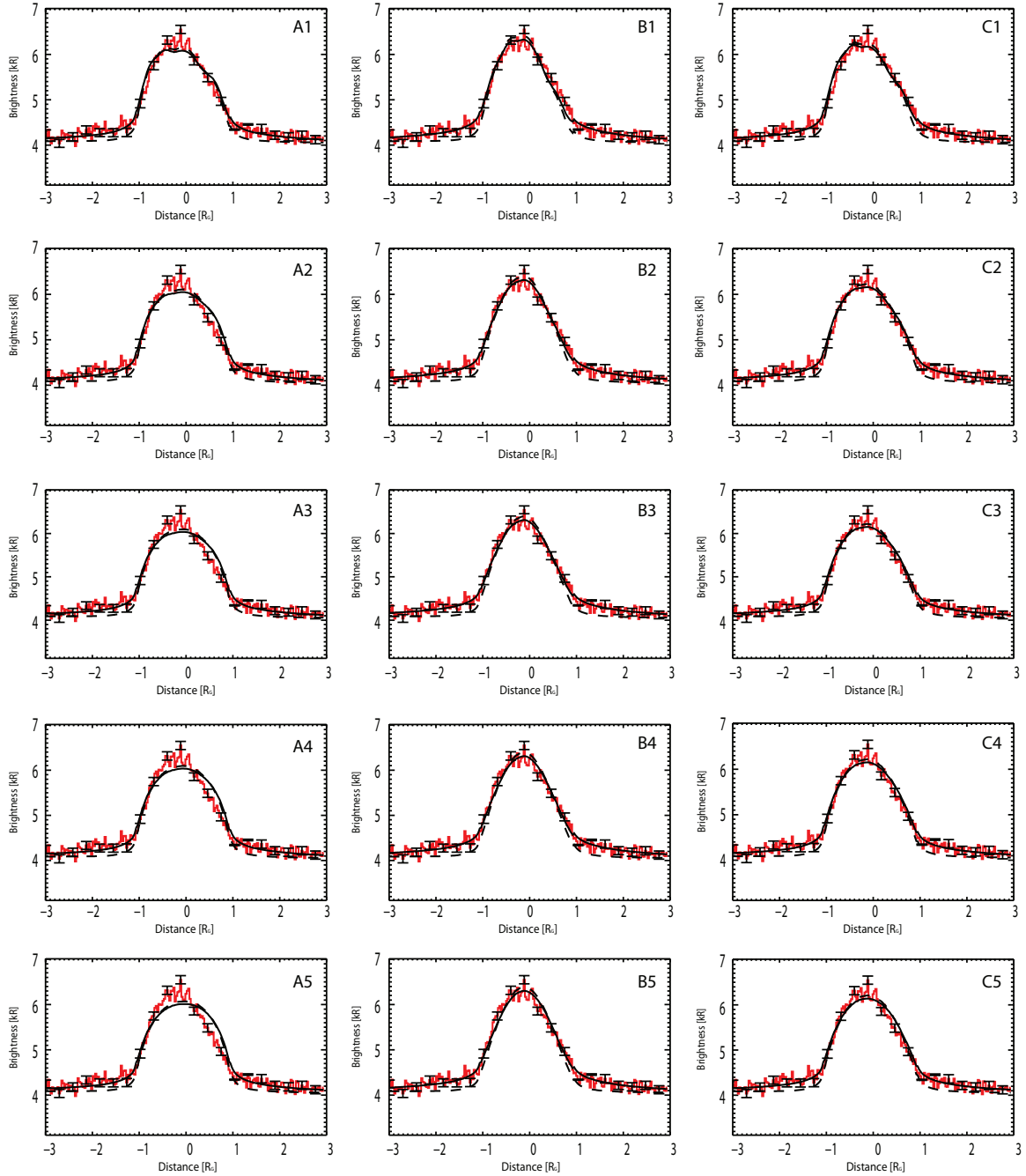


Figure 6.1: Fits of the model including (black) and not including (dashed-black) corona and the STIS profile (red) for HST Campaign 7939. The letters A-C correspond to the different phase functions presented in section 5.1.2. The numbers 1-5 correspond to the different definitions in the inversion of the inverted visible images explained in section 5.1.1.

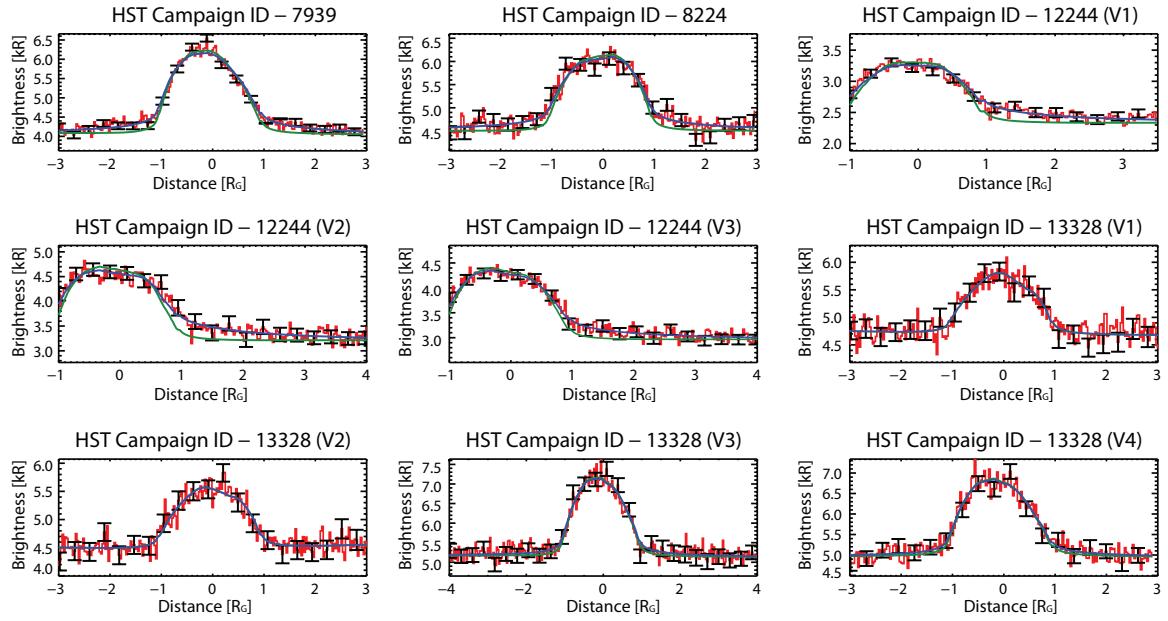


Figure 6.2: Fits of the model at Lyman- α including (blue) and not including (green) corona and the STIS profile (red) for the different HST campaigns used in this study. Error bars indicating the statistical uncertainty of the STIS profiles are included.

Table 6.1: Results derived from the analysis of Ganymede’s hydrogen corona. The extinction of the coronal emissions in the Earth’s upper atmosphere is also included.

HST Campaign ID	Surface density [cm ⁻³]	Vertical column density [cm ⁻²]	χ^2 w corona	χ^2 w/o corona	Extinction in geocorona [%]
7939	$(5.4 \pm 0.8) \times 10^3$	$(1.5 \pm 0.2) \times 10^{12}$	1.12	2.86	0
8224	$(3.4 \pm 0.8) \times 10^3$	$(9.5 \pm 2.1) \times 10^{11}$	0.86	1.48	53
12244 (V1)	$(5.4 \pm 1.5) \times 10^3$	$(1.5 \pm 0.4) \times 10^{12}$	1.04	3.18	3
12244 (V2)	$(7.9 \pm 3.0) \times 10^3$	$(2.3 \pm 0.8) \times 10^{12}$	0.75	2.02	0
12244 (V3)	$(5.8 \pm 2.3) \times 10^3$	$(1.6 \pm 0.6) \times 10^{12}$	0.85	1.95	0
13328 (V1)	$(0.2 \pm 1.3) \times 10^3$	$(0.6 \pm 3.5) \times 10^{11}$	0.93	0.93	86
13328 (V2)	$(0.0 \pm 0.4) \times 10^3$	$(0.0 \pm 1.0) \times 10^{11}$	0.75	0.75	88
13328 (V3)	$(2.5 \pm 1.7) \times 10^3$	$(6.8 \pm 4.6) \times 10^{11}$	0.74	0.80	0
13328 (V4)	$(1.9 \pm 1.6) \times 10^3$	$(5.4 \pm 4.6) \times 10^{11}$	0.85	0.90	0

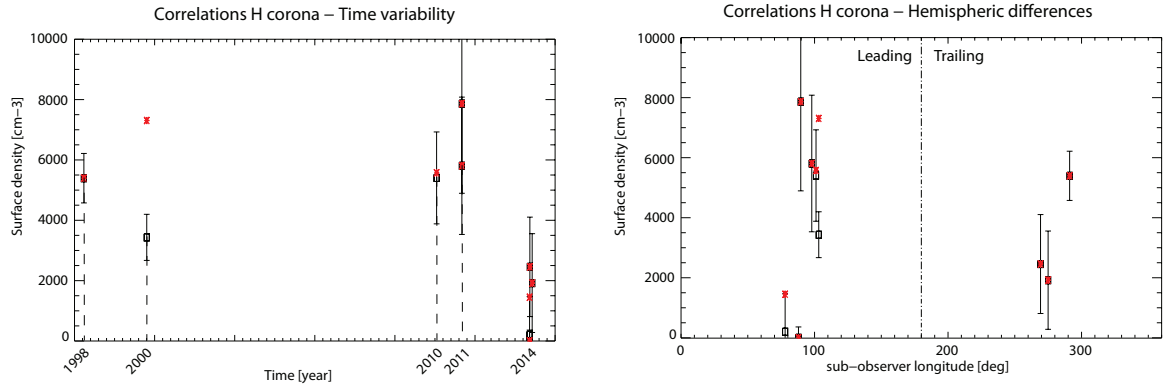


Figure 6.3: Surface density as a function of time (left) and orbital longitude (right) for the HST campaigns analyzed in this study. The black squares represent the values derived in Table 6.1. The red stars include a correction of the surface density for the extinction in the Earth’s upper atmosphere.

density has been determined from the fitting procedure, we calculate the contribution from the reflected light as:

$$I_{ref} = I_{STIS} - I_{fg} \cdot c_{fg} - I_{bg} - I_{corona}. \quad (6.0.1)$$

Then, once the brightness of the reflected sunlight in each pixel is obtained, we calculate the albedo using equation 5.1.1 (see Table 6.2).

Similarly, the albedo at different wavelengths in the FUV can be obtained from the STIS images. In particular, the STIS images in the wavelength range 1400-1700 Å are expected to represent just the solar reflected continuum, apart from a sky background. We subtract the background emission at each x pixel with the same approach as was explained in section 5.3 for the Lyman- α wavelength. We calculate Ganymede's albedo at the ranges 1410-1550 Å and 1600-1700 Å comparing the model for the reflected sunlight, and the background subtracted STIS images. In this case, we assume Ganymede behaves as a uniformly reflecting disk, as the wavelength in which the spectral inversion occurs is unknown.

The albedo is calculated using profiles along the dispersion axis, which are obtained by summing over $2R_G$ pixels in the y axis, centered at the position of the disk in the y direction (see Figure 6.4). This 1-dimensional spectrum is rebinned by 4 pixels to enhance the signal-to-noise ratio. Then, we calculate the mean value of the albedo over the different wavelength ranges using equation 5.1.1. This procedure is used for the calculation of the albedo in the ranges 1410-1550 Å and 1600-1700 Å, and the results are presented in Table 6.2.

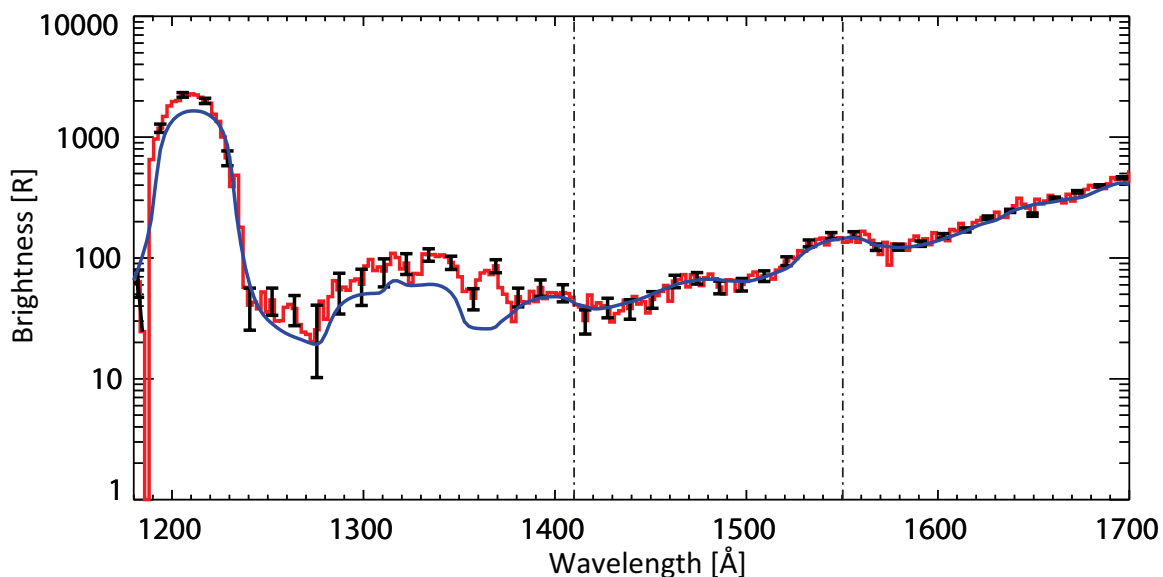


Figure 6.4: Profile in the dispersion axis obtained by summing over $2R_G$ pixels in the y axis, centered at the moon's disk in the y direction. The profile obtained after the background subtraction of the STIS images (red), represents the reflected sunlight. The solar model (blue) is scaled with the albedo in the range 1410-1550 Å, which is the range between the two dashed lines.

The orbital coverage provided by Ganymede's STIS observations makes possible the study of hemispherical difference on the albedo. Using the values for the albedo presented in Table 6.2, we fit a sinusoidal curve given by

$$p(\phi_{obs}) = a_1 + a_2 \cdot \sin(\phi_{obs}), \quad (6.0.2)$$

Table 6.2: Results for the albedo at different wavelength ranges for the different HST campaigns.

HST Campaign ID	Albedo (1215 Å) [%]	Albedo (1410-1550 Å) [%]	Albedo (1600-1700 Å) [%]
7939	3.16 ± 0.03	2.20 ± 0.29	2.33 ± 0.25
8224	1.92 ± 0.03	1.51 ± 0.29	1.61 ± 0.26
12244 (V1)	1.94 ± 0.02	1.39 ± 0.25	1.68 ± 0.23
12244 (V2)	2.15 ± 0.04	1.60 ± 0.37	1.80 ± 0.34
12244 (V3)	2.10 ± 0.03	1.36 ± 0.32	1.73 ± 0.27
13328 (V1)	1.84 ± 0.05	1.41 ± 0.41	1.75 ± 0.38
13328 (V2)	1.72 ± 0.05	1.15 ± 0.54	1.75 ± 0.41
13328 (V3)	3.00 ± 0.06	2.02 ± 0.47	2.16 ± 0.42
13328 (V4)	2.77 ± 0.06	1.76 ± 0.46	1.91 ± 0.42

where a_1 and a_2 are the parameters to fit, and ϕ_{obs} is the sub-observer longitude. The parameter a_1 represents the mean value for the albedo at the specific wavelength, and a_2 stands for the variation with respect to the mean value. Figure 6.5 shows the results obtained for the albedo at different wavelengths, including the sinusoidal function fitted by equation 6.0.2.

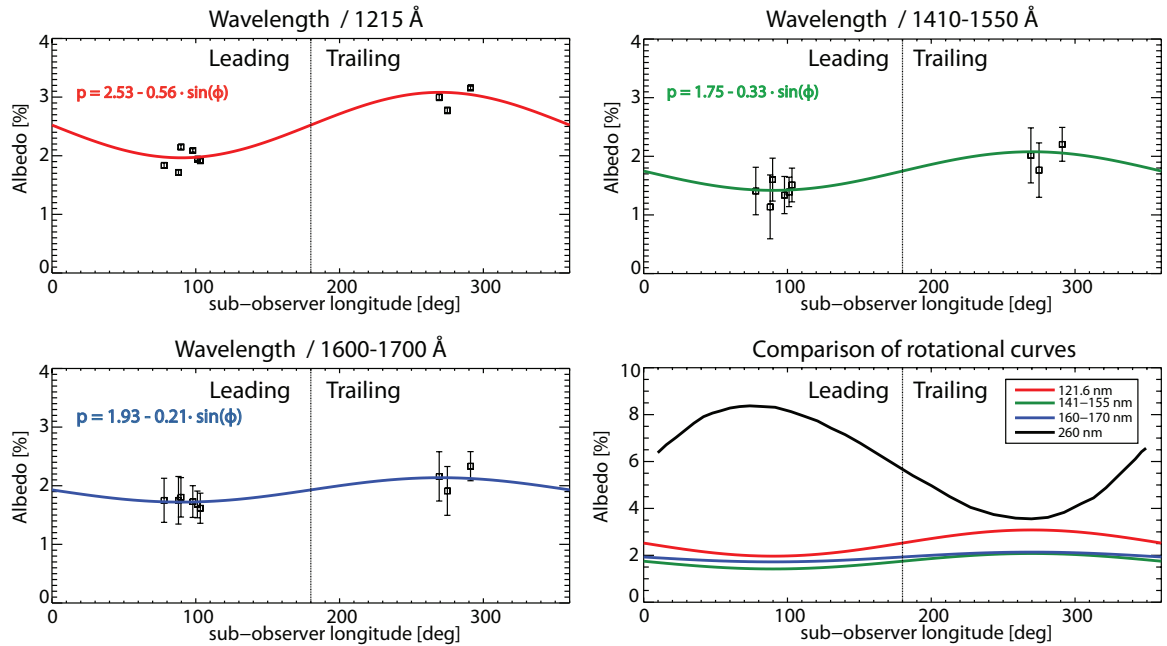


Figure 6.5: Albedo at different wavelengths with respect to the sub-observer longitude. The color lines represent the best fit for equation 6.0.2 to the albedo points derived shown in Table 6.2. The right-bottom panel shows a comparison between the three fits at different wavelength ranges, which also includes the rotational curve at 260 nm from Hendrix et al. (2005).

In conclusion, using the models presented in section 5, we have been able to represent and understand the signal observed in the STIS images. The study of the Lyman- α wavelength has allowed us to constrain the abundance of Ganymede's hydrogen corona and surface albedo. Also, the signal observed at longer wavelengths has allowed us to derive values for the albedo in the wavelength ranges 1410-1550 Å and 1600-1700 Å.

Chapter 7

Discussion

The comparison of the STIS profiles with the modeled ones at Lyman- α allow us to derive the contribution from the scattered light at Ganymede's hydrogen corona. In particular, the value of the reduced chi-squared allows us to compare the fits when including and when not including the contribution from the corona.

In HST campaigns 7939, 8224 and 12244, the detection of a hydrogen corona is clear and greater than the uncertainties. Our estimations of the signal extinction in the Earth's upper atmosphere suggest that the surface density in campaign 8224 and visit 1 in campaign 12244 might be even larger, as shown in Figure 6.3. In case of HST campaign 13328, the STIS profiles can be explained just in terms of reflected sunlight and background emissions. The results show that the detection is not statistically significant, but do not necessarily imply the non-existence of a hydrogen corona. Nevertheless, the atomic hydrogen surface density during this HST campaign seems significantly lower, as observed in Figure 6.3. In the particular case of visits 1 and 2, the extinction in the Earth's geocorona, which is approximately 85%, might explain the non-detection of Ganymede's atmospheric Lyman- α emissions.

Molyneux et al. (2017) analyzed the oxygen lines OI 1304Å and OI 1356Å for HST campaign 13328. They report that the observed intensity at these wavelengths is significantly lower than in the rest of the HST campaigns (Feldman et al., 2000; McGrath et al., 2013; Musacchio et al., 2017), which might be a result of a different magnetospheric environment. Roth et al. (2016) analyzed the oxygen auroral emissions of Europa using HST/STIS observations. Considering a stable atmosphere, and an auroral brightness proportional to the magnetospheric environment, they suggest that the lower brightnesses in the 2012-2015 period would imply a 50% lower plasma density, with respect to the 1999 period. Lower density in the magnetospheric environment could decrease the H₂O and H₂ sputtering rates, and also the dissociation rates of those molecules, leading to a decrease in the abundance of atomic hydrogen.

The results from HST campaigns 7939, 8224 and 12244, where the detection of the hydrogen corona is statistically significant, are lower by a factor of 2 on average than the value of $1.5 \times 10^4 \text{ cm}^{-3}$ reported by Barth et al. (1997). Marconi (2007) also simulated the emission due to the hydrogen corona at Lyman- α , and reported that for his model to match the results of Barth et al. (1997), he must increase the hydrogen abundance by a factor of 4. Feldman et al. (2000) analyzed the Lyman- α emission during HST campaign 7939, and reported that the emission from the extended corona outside the disk was in good agreement with the results by Barth et al. (1997). However, they did not include a model for the PSF, which can scatter

the contribution from the reflected sunlight outside the disk. Also, they fit directly the results by Barth et al. (1997), but not find the best fit providing the lowest chi-squared value.

It might seem that the surface density for the leading hemisphere is somewhat higher than for the trailing. However, due to the large error bars derived from the systematic uncertainty, it is difficult to suggest a hemispherical difference. In any case, we have looked for correlations with System Jupiter III and the true anomaly, but we did not find any apparent correlation.

Ganymede's H surface density might be compared to the results reported for the other two icy Galilean moons. Roth et al. (2017b) reported the detection of a hydrogen corona around Europa with a surface density in the range $(1.5-2.3) \times 10^3 \text{ cm}^{-3}$. In the case of Jupiter's moon Callisto, Roth et al. (2017a) reported a surface density of 2.6×10^3 for the trailing hemisphere, and $4.9 \times 10^3 \text{ cm}^{-3}$ for the leading side. In the case of Ganymede, the overall results seem to be slightly higher but comparable to the other two icy Galilean moons.

Lyman- α aurora does not appear to be present in the STIS observations of Ganymede. Roth et al. (2014) reported the presence of surpluses of Lyman- α emission coincident with emissions at the oxygen OI 130.4nm line, which imply the dissociation of H₂O. We search for potential surplus emissions at Lyman- α at the positions of brightest locations of the oxygen line (Musacchio et al., 2017; McGrath et al., 2013; Feldman et al., 2000; Molyneux et al., 2017), but we do not find any apparent correlation. Besides, the strong contribution from the reflected sunlight at Lyman- α within the disk makes difficult the isolation of potential auroral emissions.

The derived values for the albedo for the trailing hemisphere in the wavelength ranges 1410-1550 Å and 1600-1700 Å agree with the result of Feldman et al. (2000), who reported an albedo of $2.3 \pm 0.2 \%$, using the data from HST campaign 7939. Musacchio et al. (2017) presented values for the albedo in the wavelength range 1410-1550 Å of $2.7 \pm 0.4 \%$ on the trailing side and $1.8 \pm 0.4 \%$ on the leading, which are slightly higher than the results derived in this study. While the general trend of the albedo at the FUV is to decrease at shorter wavelengths, the comparison between the albedo at Lyman- α and in the range 1410-1550 Å indicate an increase. This increase at wavelengths lower than 1400 Å have also been observed at the Moon (Lucke et al., 1976; Henry et al., 1976), and are thought to be related to space weathering of the surface.

The comparison between the derived values for the albedo at Lyman- α suggest a hemispheric dichotomy between the leading and trailing hemispheres, being the latter the brightest. Although the hemispheric differences in the albedos at the wavelength range 1410-1550 Å are within the uncertainties, the systematic detection of higher values on the trailing hemisphere suggest that the trailing hemisphere is also brighter in this range. In the case of the albedo between 1600 and 1700 Å the difference between both hemispheres is relatively small, and the rotational curve presented in Figure 6.5 is practically flat. Previous photometric studies of Ganymede's surface in the MUV show that the leading hemisphere is brighter than the trailing (Noll et al., 1996; Hendrix et al., 2005), which is opposite to the observed hemispherical dichotomy on the FUV. Comparing the albedos in these wavelength ranges, the results suggest that the spectral inversion of Ganymede's surface reflectivity occurs at some point between 1600 and 2000 Å.

Chapter 8

Summary

In this thesis, we present a detailed analysis of several images of Ganymede made with the Space Telescope Imaging Spectrograph (STIS) on the Hubble Space Telescope (HST). The observations were made during several visits from 1998 to 2014, when Ganymede was located at western and eastern elongations, observing the leading and trailing hemispheres, respectively. The observational setup using the 52"x2" aperture and the G140L spectral grating provides spectrally and spatially-resolved images between 1150 and 1730 Å. We analyze the Lyman- α ($\lambda = 1216$ Å) emission in the search for a hydrogen corona around Ganymede, which was previously reported by Barth et al. (1997). We also calculate Ganymede's albedo at different wavelengths, in order to analyze how the surface reflectivity behaves in the far-ultraviolet (FUV).

We model the observed signal at Lyman- α as the result of four main contributions: scattered light in the Earth's geocorona (1), IPM (2) and Ganymede's hydrogen corona (3), apart from the reflected sunlight on Ganymede's surface (4). Besides, we include the potential extinction of the solar and IPM fluxes in Ganymede's hydrogen atmosphere.

The IPM and geocoronal emissions are properly differentiated into foreground (between HST and Ganymede) and background (between Ganymede and infinity) brightnesses, in order to not overestimate the brightness of the IPM behind Ganymede within the moon's disk. The background emissions are modeled using the approach of Pryor et al. (2008), while the foreground are calculated from regions far from the moon in the STIS images.

We consider multiple approaches for the reflected sunlight, with different models for Ganymede's surface reflectivity and phase functions. The results from the study suggest that the signal within the disk is best approximated using inverted visible images of the surface with the application of the reflectance model derived by Oren and Nayar (1994).

Ganymede's atmosphere, which is thought to be created by the sputtering and sublimation of the icy surface, is believed to possess elements from the water species, such as H₂, H or O₂ (Lanzerotti et al., 1978). Atomic hydrogen can be directly created by the sputtering of the surface, but the main sources are possibly the dissociation of H₂O and H₂ (Marconi, 2007). Hydrogen atoms are created at high speeds ($T_H \approx 1000$ K), and thus are believed to escape. We model Ganymede's hydrogen corona as an escaping exosphere, which decays as $1/r^2$ from the surface.

The model for the different sources of emission are then combined and convolved with a point spread function (PSF) for taking into account the imaging response of the system. We

compare the model and images, and detect hydrogen atmospheric emissions approximately a factor of 2 lower than the results reported by Barth et al. (1997). The surface density appears to be quite stable, but for HST campaign 13328, in which there is a substantial decrease of the density, which might be related to differences on the magnetospheric environment. We also find out that the extinction of Ganymede's coronal emissions in the Earth's upper atmosphere might be important, and thus must be estimated for a proper analysis of the results.

At wavelengths longer than 1400 Å, the signal within Ganymede's disk is expected to be solely reflected sunlight. We calculate the albedo at Lyman- α , between 1410-1550 Å, and between 1600-1700 Å. We find out that Ganymede's reflectance starts to increase for $\lambda < 1400$ Å, which might be related to space weathering processes on the surface (Lucke et al., 1976). Comparing the albedo between leading and trailing hemispheres, we find that the former is darker for $\lambda < 1600$ Å. Studies show that the leading hemisphere is brighter than the trailing for $\lambda > 2000$ Å, which is opposite to the dichotomy found for the FUV. Hence, Ganymede's surface reflectivity is spectrally inversed at some wavelength in the range 1600-2000 Å.

Appendices

Appendix A

Radiative transfer model

A.1 Extinction of solar and IPM fluxes in Ganymede's H corona

The model created to reproduce the intensity observed in the STIS images, and presented in equation 5.0.1, includes the extinction of the solar and IPM background fluxes in Ganymede's hydrogen corona. The extinction of these sources is represented by the exponential functions included in equation 5.0.1. In this section, we explain the radiative transfer model used for calculating the line-integrated cross sections σ_{IPM} and σ_{SUN} in equation 5.0.1, taking into account the line profiles and the relevant Doppler shifts.

The solar Lyman- α line profile is assumed to follow the model of Gladstone et al. (2015). This model fits the solar Lyman- α profile presented in Lemaire et al. (2005) with the sum of two equal and offset Gaussians and two equal and offset Lorentzians. Mathematically, it is given by

$$\begin{aligned} \pi F(\lambda) = & \frac{\pi F_{total}}{4\sqrt{\pi}\lambda_{dis}} \left[e^{-((\lambda-\lambda_{off}-\lambda_0)/\lambda_{dis})^2} + e^{-((\lambda+\lambda_{off}-\lambda_0)/\lambda_{dis})^2} \right] \\ & + \frac{\pi F_{total}\lambda_{dis}}{4\pi} \left[\frac{1}{\lambda_{dis}^2 + (\lambda - \lambda_{off} - \lambda_0)^2} + \frac{1}{\lambda_{dis}^2 + (\lambda + \lambda_{off} - \lambda_0)^2} \right] \end{aligned} \quad (\text{A.1.1})$$

where πF_{total} is the composite Lyman- α at Ganymede shown in Table 5.1, $\lambda_{dis} = 0.216$ Å, $\lambda_{off} = 0.220$ Å and $\lambda_0 = 1215.67$ Å.

The line profile of the IPM is produced by three different populations of hydrogen: hot solar wind atoms, hot interstellar atoms and primary interstellar atoms (Quémerais and Izmodenov, 2002). However, for the purpose of our approximation, we follow the approach of Gladstone et al. (2015) to consider a Gaussian line profile for a temperature of $T = 12000$ K, given by

$$P_\lambda d\lambda = \frac{c}{\lambda_0} \cdot \sqrt{\frac{m_H}{2\pi k_B T}} \cdot \exp\left(\frac{-m_H}{2k_B T} \left[c \left(1 - \frac{\lambda}{\lambda_0}\right) \right]^2\right) d\lambda, \quad (\text{A.1.2})$$

where $P_\lambda d\lambda$ is the fraction of particles scattering light between λ to $\lambda + d\lambda$, c is the speed of light, m_H is the mass of atomic hydrogen, k_B is the Boltzmann constant and T is the temperature. The rest of the properties considered for the abundance of atomic hydrogen in the IPM are $n = 0.12$ cm $^{-3}$, and $v = 22$ km/s, with an upstream direction at $\lambda = 252.5^\circ$ and $\beta = 8.9^\circ$ in ecliptic coordinates.

Finally, the absorption in Ganymede’s hydrogen corona is assumed to follow a Maxwellian distribution, given by equation A.1.2, with a temperature of $T_H = 1000$ K (Marconi, 2007). The absorption cross section at Lyman- α is given by

$$\sigma_\lambda = \frac{\pi e^2}{m_e c} \cdot \frac{\lambda_0^2}{c} \cdot f \cdot \phi_\lambda, \quad (\text{A.1.3})$$

where e is the electric charge, m_e is the electron mass, f is the oscillator strength at Lyman- α ($f_{Ly-\alpha} = 0.416$) and ϕ_λ is the function describing the line profile, in our case the Maxwellian distribution.

The line-center cross for a Maxwellian distribution of hydrogen at $T_H = 1000$ K is 1.86×10^{-13} cm². However, in order to estimate a more realistic value, one must also take into account the Doppler shifts and the line profiles of the sources. These behaviors can be included by calculating the line-integrated cross section.

The extinction of the source by Ganymede’s hydrogen corona is given by

$$I(\lambda) = I_0(\lambda) \cdot e^{-\sigma_\lambda N_H}. \quad (\text{A.1.4})$$

Assuming a column density of $N_H = 10^{13}$ cm⁻², which is similar to the value presented by Barth et al. (1997), one can estimate the extinction of the sources in Ganymede’s corona (see Figure A.1). Then, the line-integrated cross section can be calculated as

$$\sigma_{Ly-\alpha} = \frac{-1}{N_H} \cdot \ln \left(\frac{\int_0^\infty I(\lambda) d\lambda}{\int_0^\infty I_0(\lambda) d\lambda} \right). \quad (\text{A.1.5})$$

Table A.1 shows the results obtained for the extinction of the solar flux and IPM background emissions in Ganymede’s hydrogen corona. Apart from these results, we also make an estimation of the extinction of the solar flux in the IPM between the Earth and Ganymede, and find that approximately only 3 % of the flux will be extinct.

Table A.1: Results obtained from the radiative transfer model for the different HST campaigns. The presented values assume a column density in Ganymede’s hydrogen corona of $N_H = 10^{13}$ cm⁻², similar to the column density reported by Barth et al. (1997).

HST Campaign ID	$E_{SUN-COR}$ [%]	σ_{SUN} [cm ²]	$E_{IPM-COR}$ [%]	σ_{IPM} [cm ²]
7939	2.79	2.83×10^{-15}	0.21	2.19×10^{-16}
8224	2.84	2.88×10^{-15}	1.74	1.76×10^{-15}
12244 (V1)	2.87	2.92×10^{-15}	6.58	6.81×10^{-15}
12244 (V2-3)	2.81	2.85×10^{-15}	25.18	2.90×10^{-14}
13328 (V1)	2.83	2.88×10^{-15}	6.27	6.48×10^{-15}
13328 (V2)	2.84	2.88×10^{-15}	6.41	6.62×10^{-15}
13328 (V3)	2.83	2.87×10^{-15}	0.01	9.43×10^{-18}
13328 (V4)	2.84	2.88×10^{-15}	0.00	5.96×10^{-20}

A.2 Extinction of Ganymede’s coronal emissions in the Earth’s geocorona

Extinction of the sources of emission in the Earth’s upper atmosphere might also be significant. In order to take that factor into account, we estimate the potential extinction based on the abundance of atomic hydrogen in the Earth’s upper atmosphere.

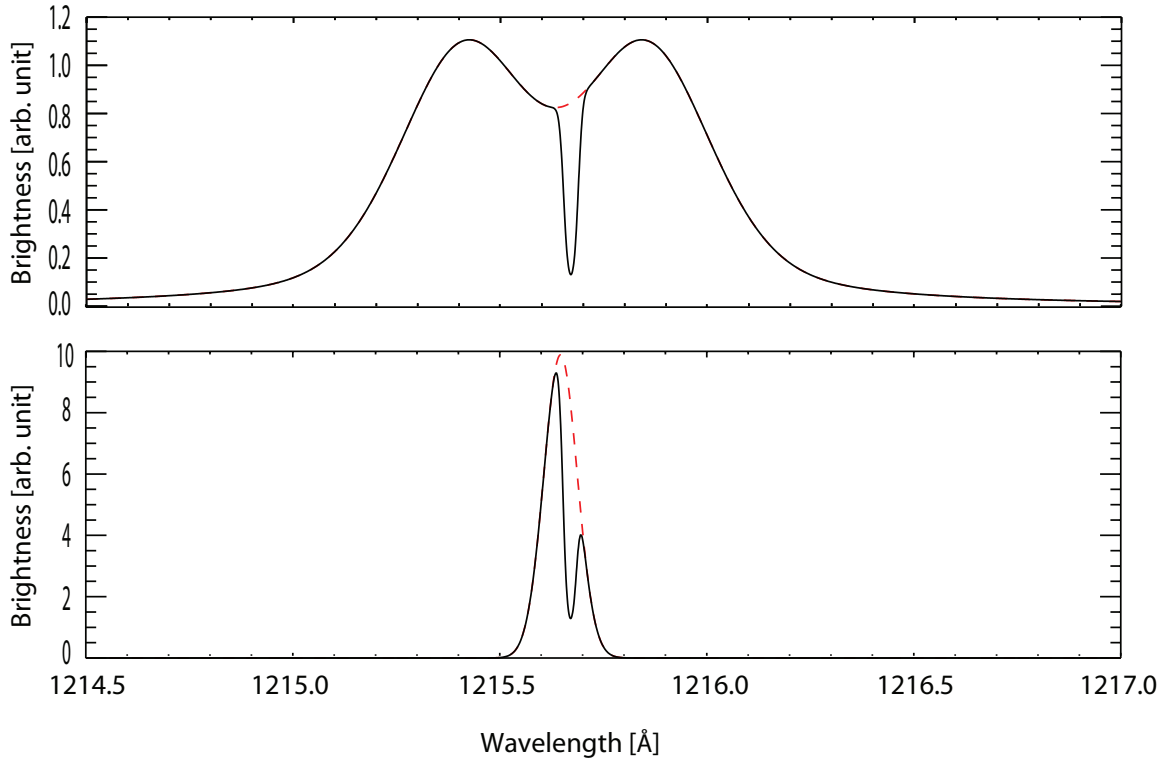


Figure A.1: Solar (top) and IPM background (bottom) line profiles expected after the extinction in Ganymede’s hydrogen corona, assuming a column density of $N_H = 10^{13} \text{ cm}^{-2}$, for HST Campaign 12244 (Visit 2). The red-dashed line represents the initial line profile, while the black line represents the line profile after extinction. All Doppler shifts are accounted for.

In order to estimate the density of atomic hydrogen in the Earth’s geocorona, we use the atmospheric model MSIS-E-90 developed by NASA (https://omniweb.gsfc.nasa.gov/vitmo/msis_vitmo.html). The model provides data for the abundance of different elements on the Earth’s atmosphere. We estimate the density of atomic hydrogen at different longitudes, latitudes and altitudes, as shown in Figure A.2.

For each of the used datasets (see Table 3.1), we calculate the positions of the HST, Ganymede, and the Doppler shift between the Earth and Ganymede at different times within the observation, using the SPICE routine. We then estimate the line-of-sight column density at each time using the data from the MSIS-E-90 model and the geometry of the observation. The top two pannels on Figure A.3 show the Doppler shift between Ganymede and the Earth, and the observed hydrogen column density, respectively.

In order to calculate the extinction, we use a similar approach than in Appendix A.1. Both Ganymede’s corona and the Earth’s geocorona are modeled using a Maxwellian distribution of $T_H = 1000 \text{ K}$, given by equation A.1.2. The absorption cross section is given by equation A.1.3, and the extinction of Ganymede’s coronal emissions are calculated as in equation A.1.4 (see Figure A.4). We apply this method at different times, obtaining a time-dependent extinction, as observed in the bottom panel of Figure A.3. Finally, in order to get an overall value for the whole HST visit, we calculate the mean value of the extinction, as presented in Table 6.1.

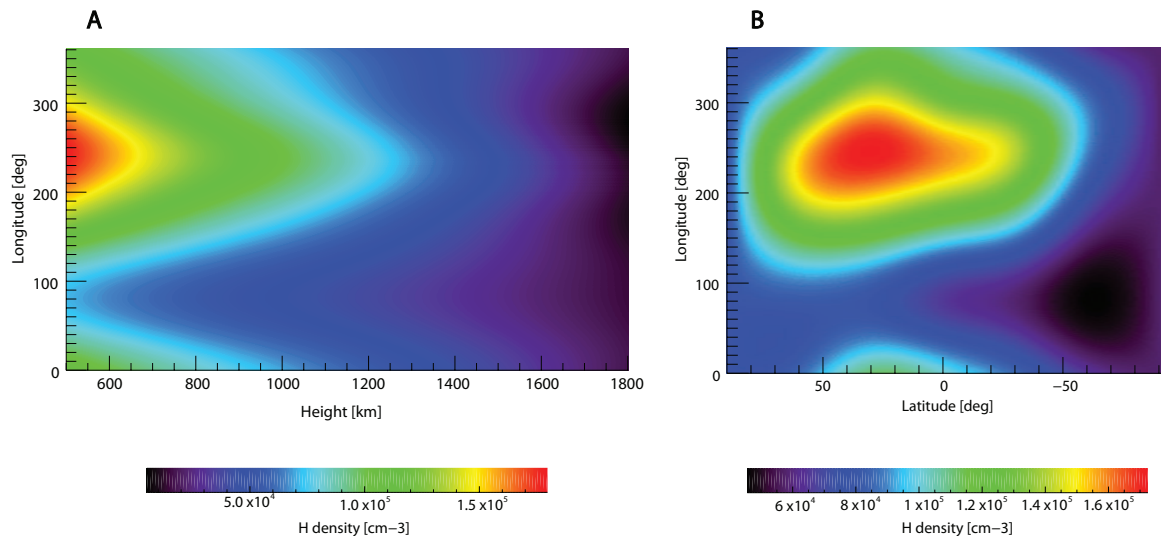


Figure A.2: Atomic hydrogen density distribution in the Earth's atmosphere for HST Campaign 7939. A) Distribution over longitude and altitude, at a constant latitude of 0 degrees. B) Distribution over longitude and latitude at a constant height of 600 km.

Atomic hydrogen density in the Earth's atmosphere appears to vary with respect to the Sun direction, being lower on the dayside than on the nightside. For our model, we consider the atmosphere to be static at the middle of the each HST visit. The change of the atmospheric properties during the exposure time is most important during visit 1 in HST campaign 12244, which takes approximately 6 hours and 30 minutes. However, we estimate the systematic error by considering the atmosphere at different times during the observation, and find that for that HST campaign the results would change approximately in a range of $3 \pm 0.5\%$.

The greater dependency of the extinction in the Earth's upper atmosphere is due to the Doppler shift between the HST and Ganymede. Considering both Ganymede's and Earth's hydrogen atmospheres to have $T = 1000$ K, a Doppler shift lower than approximately 15 km/s will produce extinction of the signal. Indeed, the main difference between the extinction in the Earth's upper atmosphere for the various HST campaigns is due to the Doppler shift, rather than the line-of-sight column density.

Some characteristics about the relation between HST's motion and the extinction in the Earth's hydrogen atmosphere can also be inferred from Figure A.3. Usually, each visit is composed of various orbits, which include two datasets per orbit. Apart from the first orbit of the visit, the first dataset in each orbit is characterized by a large line-of-sight column density, which also corresponds to the datasets we discarded in section 4 due to the stronger geocoronal emissions. On the other hand, the second dataset in each orbit is characterized by a lower line-of-sight column density, indicating that the HST is approaching its closest point to Ganymede.

In conclusion, the extinction of Ganymede's atmospheric Lyman- α emission in the Earth's upper atmosphere can be important if the Doppler shift between the Earth and Ganymede is lower than ≈ 15 km/s. We have shown that in some cases the extinction of the signal can be up to 85%, and thus is an important effect to take into account in future studies.

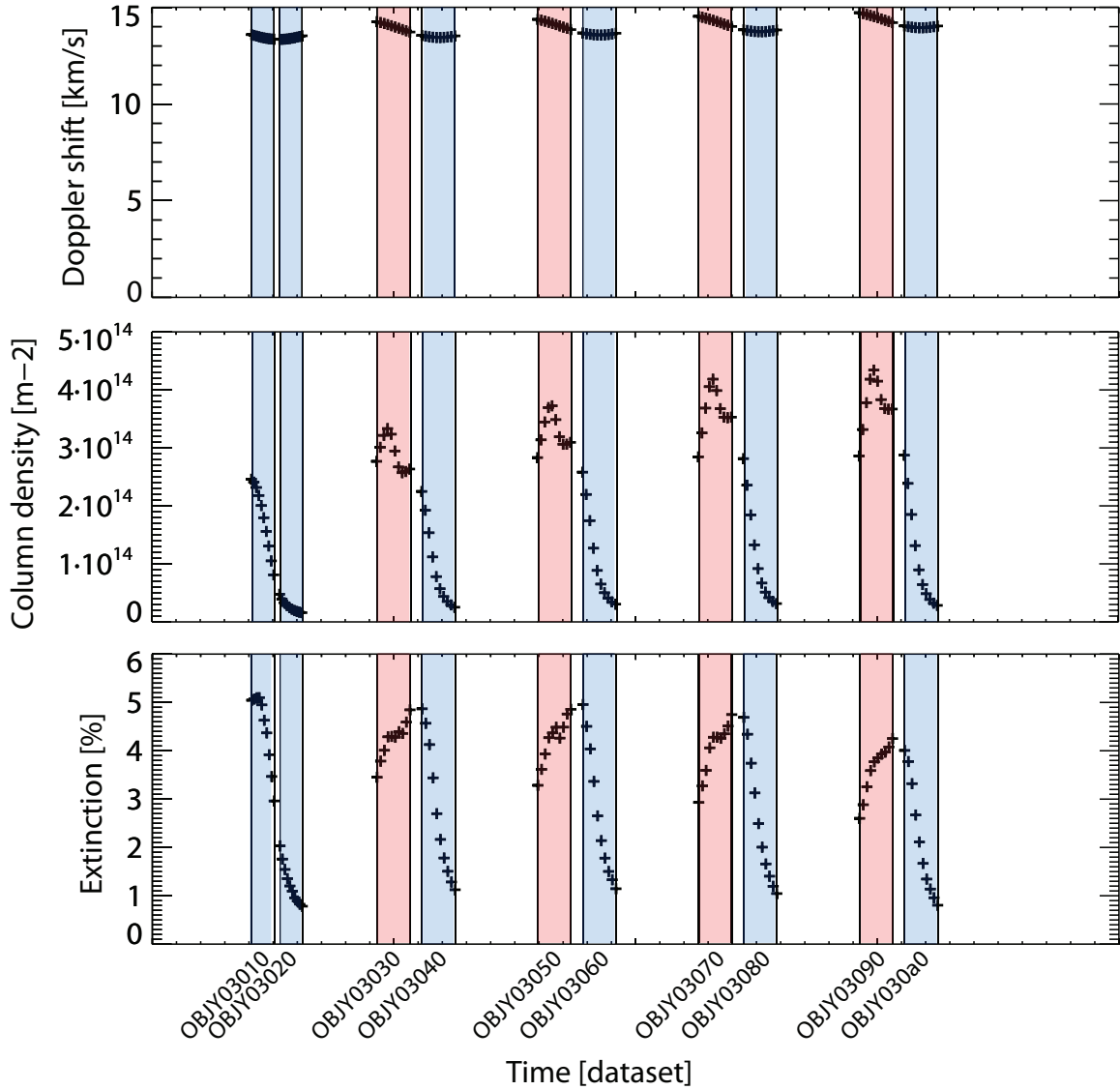


Figure A.3: Extinction of Ganymede's Lyman- α coronal emissions as a function of time during HST campaign 12244 (V1). The three panels show the Doppler shift between the moon and the Earth, the line-of-sight H density and the extinction during exposure time of the observations. These plots show evolution for every dataset in the visit. The datasets we consider in this thesis are shadowed in blue.

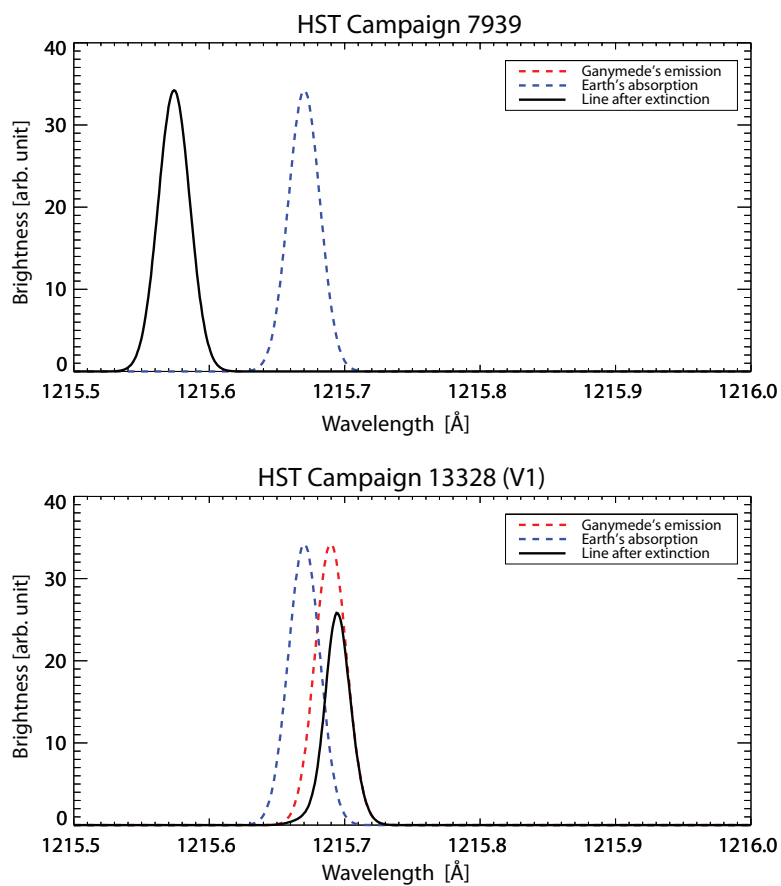


Figure A.4: Extinction of Ganymede's Lyman- α coronal emissions in the Earth's upper atmosphere for HST Campaign 7939 and 13328 (V1), respectively. It can be observed that when the Doppler shift between the moon and the HST is small, Ganymede's coronal emissions will be extinct in the geocorona.

Appendix B

Derivations for the radially escaping H corona

B.1 Density distribution function

The continuity equation for number density expresses that the rate of change of the particle density may be equal to the flow entering or leaving the volume, in the absence of sources or losses:

$$\frac{\partial n_n}{\partial t} + \nabla \cdot (n_n \mathbf{u}) = 0 \quad (\text{B.1.1})$$

where n_n is the particle density of neutrals and \mathbf{u} is the flow velocity.

Assuming a stationary case, the temporal derivative vanishes, which gives:

$$\nabla \cdot (n_n \mathbf{u}) = 0 \quad (\text{B.1.2})$$

In spherical components, the divergence of a vector is given by:

$$\nabla \cdot \mathbf{A} = \frac{1}{r^2} \frac{\partial(r^2 A_r)}{\partial r} + \frac{1}{r \sin \theta} \frac{\partial(A_\theta \sin \theta)}{\partial \theta} + \frac{1}{r \sin \theta} \frac{\partial A_\varphi}{\partial \varphi} \quad (\text{B.1.3})$$

Assuming spherical symmetry, the dependencies with the azimuthal and polar angles vanish. Then, applying equation B.1.3 to equation B.1.2:

$$\frac{1}{r^2} \frac{\partial(r^2 n(r) u_r)}{\partial r} = 0 \quad \longrightarrow \quad r^2 n(r) u_r = K \quad (\text{B.1.4})$$

where K is a constant. Considering a constant flow velocity in the r direction u_r , then:

$$r^2 n(r) = K' \quad (\text{B.1.5})$$

where K' is another constant. Finally, using the boundary condition $n(r = R_C) = n_0$, one gets:

$$n(r) = n_0 \left(\frac{R_G}{r} \right)^2 \quad (\text{B.1.6})$$

which represents the number density dependence with the distance to the surface of the moon.

B.2 Column density distribution function

The definition of the column density is given by:

$$N(r) = \int n(r) dr \quad (\text{B.2.1})$$

In order to calculate the line-of-sight column density, a geometry like shown in Figure B.1 should be considered. In such a case, it is possible to define $r^2 = x^2 + y^2$. As the name implies, the integration must be performed over the line of sight direction, which in this geometry corresponds to the x axis. Then, introducing the equation B.1.6:

$$N(y) = \int n(x, y) dx = n_0 R_G^2 \int_{x_1}^{x_2} \frac{1}{x^2 + y^2} dx \quad (\text{B.2.2})$$

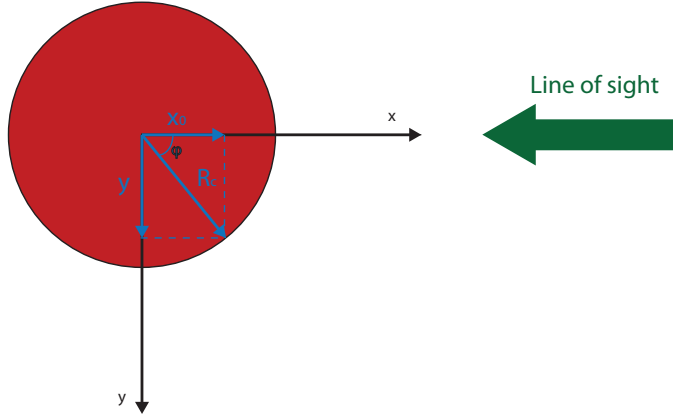


Figure B.1: Geometry considered for the integration of the number density in order to obtain the line-of-sight column density.

Such an integral is solved by considering the change of variable $x = y \tan \theta$, which implies that $\theta = \tan^{-1}(x/y)$ and $dx = y \cdot \sec^2 \theta \cdot d\theta$:

$$\begin{aligned} N(y) &= n_0 R_G^2 \int_{x_1}^{x_2} \frac{1}{x^2 + y^2} dx = n_0 \frac{R_G^2}{y^2} \int_{x_1}^{x_2} \frac{1}{1 + \frac{x^2}{y^2}} dx \\ &= n_0 \frac{R_G^2}{y^2} \int_{\theta(x_1)}^{\theta(x_2)} \frac{1}{1 + \tan^2 \theta} \cdot y \cdot \sec^2 \theta \cdot d\theta \\ &= n_0 \frac{R_G^2}{y} \int_{\theta(x_1)}^{\theta(x_2)} \frac{1}{\sec^2 \theta} \cdot \sec^2 \theta \cdot d\theta = n_0 \frac{R_G^2}{y} [\theta]_{\theta(x_1)}^{\theta(x_2)} \end{aligned} \quad (\text{B.2.3})$$

Then, changing again θ by x , the final expression for the integral states:

$$N(y) = n_0 \frac{R_G^2}{y} \left[\tan^{-1} \left(\frac{x}{y} \right) \right]_{x_1}^{x_2} \quad (\text{B.2.4})$$

At this point, it is useful to define the relations between (x, y) and the polar coordinates (r, φ) as $x = r \cos \varphi$ and $y = r \sin \varphi$. Then, one can write:

$$\begin{aligned} N(y) &= n_0 \frac{R_G^2}{y} \left[\tan^{-1} \left(\frac{\cos \varphi}{\sin \varphi} \right) \right]_{\varphi(x_1)}^{\varphi(x_2)} \\ &= n_0 \frac{R_G^2}{y} \left[\tan^{-1}(\cotan \varphi) \right]_{\varphi(x_1)}^{\varphi(x_2)} \end{aligned} \quad (\text{B.2.5})$$

Including the trigonometric relation $\cotan(x) = \tan(\frac{\pi}{2} - x)$:

$$\begin{aligned} N(y) &= n_0 \frac{R_G^2}{y} \left[\tan^{-1} \left(\tan \left(\frac{\pi}{2} - \varphi \right) \right) \right]_{\varphi(x_1)}^{\varphi(x_2)} \\ &= n_0 \frac{R_G^2}{y} \left[\frac{\pi}{2} - \varphi \right]_{\varphi(x_1)}^{\varphi(x_2)} \\ &= n_0 \frac{R_G^2}{y} (\varphi(x_1) - \varphi(x_2)) \end{aligned} \quad (\text{B.2.6})$$

The next step consists in determining the integration limits, taking into account the difference when $y > R_G$ and $y \leq R_G$. In the first case, the integration limits are from $x_1 = -\infty$ to $x_2 = \infty$. However, in the second case the lower limit is given at the surface, by the expression $x_1 = \sqrt{R_C^2 - y^2}$, while the second limit is also given by $x_2 = \infty$.

Taking into account the geometry given by Figure B.1, the integration limits for the polar angle φ are: $\varphi \rightarrow 0$ when $x \rightarrow \infty$; $\varphi \rightarrow \pi$ when $x \rightarrow -\infty$; and $\varphi \rightarrow \arcsin(y/R_G)$ when $x \rightarrow x_0$. Then one can obtain:

$$\begin{aligned} N(y > R_G) &= n_0 \frac{R_G^2}{y} (\varphi(x \rightarrow -\infty) - \varphi(x \rightarrow +\infty)) \\ &= n_0 \frac{R_G^2}{y} (\pi - 0) \\ &= n_0 \frac{R_G^2}{y} \pi \end{aligned} \quad (\text{B.2.7})$$

$$\begin{aligned} N(y \leq R_G) &= n_0 \frac{R_C^2}{y} (\varphi(x \rightarrow x_0) - \varphi(x \rightarrow +\infty)) \\ &= n_0 \frac{R_C^2}{y} (\arcsin(y/R_G) - 0) \\ &= n_0 \frac{R_C^2}{y} \arcsin\left(\frac{y}{R_G}\right) \end{aligned} \quad (\text{B.2.8})$$

If the symmetry of the system is taken into account, a more general expression can be obtained:

$$N(r) = \begin{cases} n_0 \frac{R_G^2}{r} \arcsin\left(\frac{r}{R_G}\right) & \text{if } r \leq R_G \\ n_0 \frac{R_G^2}{r} \pi & \text{if } r > R_G \end{cases} \quad (\text{B.2.9})$$

Appendix C

Error analysis

The model, as well as the signal detected by STIS, has some statistical uncertainties that one must take into account. This process is specially important considering that the model and STIS images are compared by a fitting procedure in section 6, in which the fit is weighted taking into account the error associated with each pixel. Therefore, it is important to properly derive the propagation of errors.

In our study, we present results for the abundance of atomic hydrogen in Ganymede's atmosphere, as well as the geometric albedo.

In the case of the uncertainty associated with the atomic hydrogen surface density, we need to consider both statistical and systematic errors. The statistical uncertainty is given by the standard deviation calculated with the MPFIT routine in IDL. Regarding the systematic error found in our analysis, it originates in the differences between the surface density when considering different approaches for the reflected sunlight. We consider the systematic uncertainty to be equal to the difference between the reported result and the values obtained in the approaches with a reduced chi-squared lower than 1.2.

Regarding the uncertainty associated with the geometric albedo, one must consider the error propagation, as the calculated reflected sunlight in equation 6.0.1 depends on different quantities. Bevington and Robinson (2003) shows that the error associated with a quantity which is a function of other variables $x = f(u, v, \dots)$ can be approximated by

$$\sigma_x^2 \approx \sigma_u^2 \cdot \left(\frac{\delta x}{\delta u}\right)^2 + \sigma_v^2 \cdot \left(\frac{\delta x}{\delta v}\right)^2, \quad (\text{C.0.1})$$

where σ_x , σ_u and σ_v are the standard deviations of the different quantities. Taking into account equations 6.0.1 and C.0.1, and neglecting the uncertainty of the IPM background emission, the uncertainty of the reflected sunlight in Rayleigh is given by

$$\sigma_{ref} = k_{unit} \cdot \sqrt{\sigma_0^2 + \sigma_{fg}^2 + \sigma_{corona}^2} \quad (\text{C.0.2})$$

where σ_0 is the standard deviation of the observed signal I_0 , which is given in the STIS files; σ_{fg} is the statistical uncertainty of the foreground emission; σ_{corona} is the error in the emission from Ganymede's hydrogen corona; and k_{unit} stands for the conversion between counts and brightness in Rayleigh.

We calculate the error of the foreground emission as the square root of the foreground counts, which are assumed to follow a Poisson distribution, as

$$\sigma_{fg} = \sqrt{\frac{I_{fg}}{k_{unit}}} \quad (\text{C.0.3})$$

where the resulting σ_{fg} has the units of counts and I_{fg} is the foreground emission in each pixel.

In the case of the uncertainty of the coronal emissions, they are simply obtained by

$$\sigma_{corona} = \frac{1}{k_{unit}} \cdot 10^{-6} \cdot g \cdot \sigma_{N_H}, \quad (\text{C.0.4})$$

where σ_{N_H} includes both the statistical and systematic uncertainties of the derived hydrogen corona.

Thus, with this definitions we are able to calculate the uncertainty associated with the reflected sunlight observed in the STIS images. The uncertainty of the geometric albedo can then be calculated using equations 5.1.1 and C.0.1, and is given by

$$\sigma_p \approx \sqrt{\sigma_{ref}^2 \cdot \frac{1}{I_{SUN}^2} + \sigma_{SUN}^2 \cdot \frac{I_{REF}^2}{I_{SUN}^4}} \quad (\text{C.0.5})$$

where I_{SUN} stands for the incident sunlight, but including the different constants in equation 5.1.1. Although the error in the solar flux is not known, we assume an uncertainty of 20% due to possible variations within the same day.

In conclusion, we have derived uncertainties for the main results that we present in this study. The total error of the hydrogen surface density is composed of both systematic and statistical errors. In the case of the uncertainty in the albedo, we consider the error propagation to calculate the total uncertainty.

Bibliography

- Anderson, J. D., Lau, E. L., Sjogren, W. L., Schubert, G., and Moore, W. B. (1996). Gravitational constraints on the internal structure of Ganymede. *Nature*, 384(6609):541–543.
- Barth, C. A., Hord, C. W., Stewart, A. I. F., Pryor, W. R., Simmons, K. E., McClintock, W. E., Ajello, J. M., Naviaux, K. L., and Aiello, J. J. (1997). Galileo ultraviolet spectrometer observations of atomic hydrogen in the atmosphere of Ganymede. *Geophysical Research Letters*, 24(17):2147–2150.
- Bevington, P. R. and Robinson, D. K. (2003). *Data Reduction and Error Analysis for the Physical Sciences*. McGraw-Hill, New York, NY.
- Bland, M. T., Showman, A. P., and Tobie, G. (2008). The production of Ganymede’s magnetic field. *Icarus*, 198(2):384–399.
- Bostroem, K. a. (2010). Space Telescope Imaging Spectrograph Instrument Handbook for Cycle 19. *Baltimore: STScI*, (January):1–514.
- Brown, M. (1997). A Search for a Sodium Atmosphere around Ganymede. *Icarus*, 126(1):236–238.
- Brown, W. L., Lanzerotti, L. J., Poate, J. M., and Augustyniak, W. M. (1978). "Sputtering" of Ice by MeV Light Ions. *Physical Review Letters*, 40(15):1027–1030.
- Buratti, B. J. (1991). Ganymede and Callisto: Surface textural dichotomies and photometric analysis. *Icarus*, 92(2):312–323.
- Carlson, R. W., Bhattacharyya, J. C., Smith, B. A., Johnson, T. V., Hidayat, B., Smith, S. A., Taylor, G. E., O’Leary, B., and Brinkmann, R. T. (1973). An Atmosphere on Ganymede from Its Occultation of SAO 186800 on 7 June 1972. *Science*, 182(4107):53 LP – 55.
- Chamberlain, J. W. and Hunten, D. M. (1987). *Theory of Planetary Atmospheres. An Introduction to their Physics and Chemistry*. Academic Press Inc., Orlando, FL, USA.
- Cooper, J. F., Johnson, R. E., Mauk, B. H., Garrett, H. B., and Gehrels, N. (2001). Energetic ion and electron irradiation of the icy Galilean satellites. *Icarus*, 149:133–159.
- Domingue, D. and Verbiscer, A. (1997). Re-analysis of the solar phase curves of the icy Galilean satellites. *Icarus*, 128(1):49–74.
- Emerich, C., Lemaire, P., Vial, J. C., Curdt, W., Schühle, U., and Wilhelm, K. (2005). A new relation between the central spectral solar H I Lyman α irradiance and the line irradiance measured by SUMER/SOHO during the cycle 23. *Icarus*, 178(2):429–433.

- Eviatar, A., Strobel, D. F., Wolven, B. C., Feldman, P. D., Mcgrath, M. A., and Williams, D. J. (2001). Excitation of the Ganymede Ultraviolet Aurora. *The Astrophysical Journal*, 555(2):1013.
- Feldman, P. D., McGrath, M. A., Strobel, D. F., Moos, H. W., Retherford, K. D., and Wolven, B. C. (2000). HST/STIS Ultraviolet Imaging of Polar Aurora on Ganymede. *The Astrophysical Journal*, 535(2):1085.
- Gladstone, G. R., Pryor, W. R., and Alan Stern, S. (2015). Lyman-alpha at Pluto. *Icarus*, 246:279–284.
- Gurnett, D. A., Kurth, W. S., Roux, A., Bolton, S. J., and Kennel, C. F. (1996). Evidence for a magnetosphere at Ganymede from plasma-wave observations by the Galileo spacecraft. *Nature*, 384(6609):535–537.
- Hall, D. T., Feldman, P. D., McGrath, M. A., and Strobel, D. F. (1998). The FarUltraviolet Oxygen Airglow of Europa and Ganymede. *The Astrophysical Journal*, 499(1):475–481.
- Hansen, G. B. and McCord, T. B. (2004). Amorphous and crystalline ice on the Galilean satellites: A balance between thermal and radiolytic processes. *European Planetary Science Congress*, 109(E1):2.
- Hapke, B. (2012). *Theory of Reflectance and Emittance Spectroscopy*.
- Hendrix, A. R., Domingue, D. L., and King, K. (2005). The icy Galilean satellites: ultraviolet phase curve analysis. *Icarus*, 173(1):29–49.
- Henry, R. C., Fastie, W. G., Lucke, R. L., and Hapke, B. W. (1976). A far-ultraviolet photometer for planetary surface analysis. *The Moon*, 15(1-2):51–65.
- Hibbitts, C. A., Pappalardo, R. T., Hansen, G. B., and McCord, T. B. (2003). Carbon dioxide on Ganymede. *Journal of Geophysical Research*, 108(E5):5036.
- Hunten, D., Roach, F., and Chamberlain, J. (1956). A photometric unit for the airglow and aurora. *Journal of Atmospheric and Terrestrial Physics*, 8(6):345–346.
- Johnson, R. E., Combi, M. R., Fox, J. L., Ip, W.-H., Leblanc, F., McGrath, M. A., Shematovich, V. I., Strobel, D. F., and Waite, J. H. (2008). Exospheres and Atmospheric Escape. *Space Science Reviews*, 139(1-4):355–397.
- Karttunen, H., Kröger, P., Oja, H., Poutanen, M., and Donner, K. J., editors (2007). *Fundamental Astronomy*. Springer Berlin Heidelberg, Berlin, Heidelberg.
- Kivelson, M. G., Khurana, K. K., Russell, C. T., Walker, R. J., Warnecke, J., Coroniti, F. V., Polanskey, C., Southwood, D. J., and Schubert, G. (1996). Discovery of Ganymede’s magnetic field by the Galileo spacecraft. *Nature*, 384(6609):537–541.
- Kivelson, M. G., Khurana, K. K., and Volwerk, M. (2002). The Permanent and Inductive Magnetic Moments of Ganymede. *Icarus*, 157:507–522.
- Krist, J. E., Hook, R. N., and Stoehr, F. (2011). 20 years of Hubble Space Telescope optical modeling using Tiny Tim. 8127:16.
- Lanzerotti, L. J., Brown, W. L., Poate, J. M., and Augustyniak, W. M. (1978). On the contribution of water products from Galilean satellites to the Jovian magnetosphere. *Geophysical Research Letters*, 5(2):155–158.

- Lemaire, P., Emerich, C., Vial, J.-C., Curdt, W., Schühle, U., and Wilhelm, K. (2005). Variation of the full Sun hydrogen Lyman profiles through solar cycle 23. *Advances in Space Research*, 35(3):384–387.
- Lucke, R. L., Henry, R. C., and Fastie, W. G. (1976). Far-ultraviolet albedo of the Moon. *The Astronomical Journal*, 81(12).
- Marconi, M. (2007). A kinetic model of Ganymede’s atmosphere. *Icarus*, 190(1):155–174.
- Martin, S. and Baltimore, D. (2011). *STIS Data Handbook*. Number May.
- McCord, T. B., Carlson, R. W., Smythe, W. D., Hansen, G. B., Clark, R. N., Hibbitts, C. A., Fanale, F. P., Granahan, J. C., Segura, M., Matson, D. L., Johnson, T. V., and Martin, P. D. (1997). Organics and Other Molecules in the Surfaces of Callisto and Ganymede. *Science*, 278(5336):271 LP – 275.
- McCord, T. B., Hansen, G. B., and Hibbitts, C. A. (2001). Hydrated Salt Minerals on Ganymede’s Surface: Evidence of an Ocean below. *Science*, 292(5521):1523–1525.
- McGrath, M. A., Hansen, C. J., and Hendrix, A. R. (2009). *Europa*. University of Arizona Press.
- McGrath, M. A., Jia, X., Retherford, K., Feldman, P. D., Strobel, D. F., and Saur, J. (2013). Aurora on Ganymede. *Journal of Geophysical Research: Space Physics*, 118(5):2043–2054.
- Molyneux, P. M., Nichols, J. D., Bannister, N. P., Bunce, E. J., Clarke, J. T., Cowley, S. W. H., Gérard, J.-C., Grodent, D., Milan, S. E., and Paty, C. (2017). Hubble Space Telescope observations of hemispheric and temporal variations in Ganymede’s oxygen atmosphere and aurora. Magnetospheres of the Outer Planets Conference.
- Musacchio, F., Saur, J., Roth, L., Retherford, K. D., Mcgrath, M. A., Feldman, P. D., and Strobel, D. F. (2017). Morphology of Ganymede ’ s FUV auroral ovals. *Journal of Geophysical Research : Space Physics*, pages 1–22.
- Nelson, R. M., Lane, A. L., Matson, D. L., Veeder, G. J., Buratti, B. J., and Tedesco, E. F. (1987). Spectral geometric albedos of the Galilean satellites from 0.24 to 0.34 micrometers: Observations with the international ultraviolet explorer. *Icarus*, 72(2):358–380.
- Noll, K. S., Johnson, R. E., Lane, A. L., Domingue, D. L., and A, H. (1996). Detection of Ozone on Ganymede. *Science*, 273(5273):341–343.
- Oren, M. and Nayar, S. K. (1994). Generalization of Lambert’s reflectance model. In *Proceedings of the 21st annual conference on Computer graphics and interactive techniques - SIGGRAPH ’94*, pages 239–246, New York, New York, USA. ACM Press.
- Pappalardo, R. T., Collins, G. C., Head, J. W., Helfenstein, P., McCord, T. B., Moore, J. M., Prockter, L. M., Schenk, P. M., and Spencer, J. R. (2004). Geology of Ganymede. In Bagenal, F., Dowling, T., and McKinnon, W. B., editors, *Jupiter: The Planet, Satellites and Magnetosphere*, chapter 16, pages 363–391. Cambridge University Press.
- Prockter, L. M., Figueredo, P. H., Pappalardo, R. T., Head, J. W., and Collins, G. C. (2000). Geology and mapping of dark terrain on Ganymede and implications for grooved terrain formation. *Journal of Geophysical Research: Planets (1991–2012)*, 105(E9):22519–22540.

- Prockter, L. M., Head, J. W., Pappalardo, R. T., Senske, D. A., Neukum, G., Wagner, R., Wolf, U., Oberst, J. O., Giese, B., Moore, J. M., Chapman, C. R., Helfenstein, P., Greeley, R., Breneman, H., and Belton, M. J. (1998). Dark Terrain on Ganymede: Geological Mapping and Interpretation of Galileo Regio at High Resolution. *Icarus*, 135(1):317–344.
- Pryor, W., Gangopadhyay, P., Sandel, B., Forrester, T., Quemerais, E., Möbius, E., Esposito, L., and Stewart, I. (2008). Special feature Radiation transport of heliospheric Lyman- α from combined Cassini and Voyager data sets. 28:21–28.
- Quémerais, E. and Izmodenov, V. V. (2002). Effects of the heliospheric interface on the interplanetary Lyman- α glow seen at 1 AU from the Sun. *Astronomy & Astrophysics*, 396:269–281.
- Roth, L. (2012). Aurorae of Io and Europa: Observations and Modelling.
- Roth, L., Alday, J., Becker, T. M., Ivchenko, N., and Retherford, K. D. (2017a). Detection of a hydrogen corona at Callisto. *Journal of Geophysical Research: Planets*.
- Roth, L., Retherford, K. D., Ivchenko, N., Schlatter, N., Strobel, D. F., Becker, T. M., and Grava, C. (2017b). Detection of a Hydrogen Corona in HST Ly- α Images of Europa in Transit of Jupiter. *The Astronomical Journal*, 153(2):67.
- Roth, L., Saur, J., Retherford, K. D., Strobel, D. F., Feldman, P. D., McGrath, M. A., and Nimmo, F. (2014). Transient Water Vapor at Europa’s South Pole. *Science*, 343(6167):171–174.
- Roth, L., Saur, J., Retherford, K. D., Strobel, D. F., Feldman, P. D., McGrath, M. A., Spencer, J. R., Blöcker, A., and Ivchenko, N. (2016). Europa’s far ultraviolet oxygen aurora from a comprehensive set of HST observations. *Journal of Geophysical Research A: Space Physics*, 121(3):2143–2170.
- Saur, J., Duling, S., Roth, L., Jia, X., Strobel, D. F., Feldman, P. D., Christensen, U. R., Retherford, K. D., McGrath, M. A., Musacchio, F., Wennmacher, A., Neubauer, F. M., Simon, S., and Hartkorn, O. (2015). The search for a subsurface ocean in Ganymede with Hubble Space Telescope observations of its auroral ovals. *Journal of Geophysical Research: Space Physics*, 120(3):1715–1737.
- Seifert, C., Mandt, K., Retherford, K. D., Greathouse, T. K., Hendrix, A. R., Egan, A., Gladstone, G. R., Feldman, P. D., Grava, C., and Miles, P. (2014). LRO Lyman Alpha Mapping Project (LAMP) Investigation of the Lunar Albedo Far-UV Spectral Inversion. The Woodlands, Houston, TX, USA. 45th Lunar and Planetary Science Conference.
- Showman, A. P. and Malhotra, R. (1999). The Galilean Satellites. *Science*, 286(5437):77–84.
- Spencer, J. R. (1987). The Surfaces of Europa, Ganymede, and Callisto: an Investigation Using Voyager IRIS Thermal Infrared Spectra.
- Spencer, J. R., Calvin, W. M., and Person, M. J. (1995). Charge-coupled device spectra of the Galilean satellites: Molecular oxygen on Ganymede. *Journal of Geophysical Research: Planets*, 100(E9):19049–19056.
- Spencer, J. R. and Robert, J. (1987). The Surfaces of Europa, Ganymede, and Callisto: an Investigation Using Voyager IRIS Thermal Infrared Spectra. *Thesis (PH.D.)—THE UNIVERSITY OF ARIZONA, 1987*. Source: *Dissertation Abstracts International, Volume: 48-03, Section: B, page: 0793*.

Yung, Y. and McElroy, M. (1977). Stability of an oxygen atmosphere on ganymede. *Icarus*, 30(1):97-103.

TRITA EE 2017:078